2021-12-17

An Analysis of Two Photometric Redshift Methods and Their Uses for Finding Void Galaxies

Rochelle J. Steele
Brigham Young University

An Analysis of Two Photometric Redshift Methods and Their Uses for Finding Void Galaxies

Rochelle J. Steele

A thesis submitted to the faculty of
Brigham Young University
in partial fulfillment of the requirements for the degree of

Master of Science

J. Ward Moody, Chair
Michael Joner
Eric Hintz
Christian Draper

Department of Physics and Astronomy

Brigham Young University

ABSTRACT

An Analysis of Two Photometric Redshift Methods and Their Uses for Finding Void Galaxies

Rochelle J. Steele
Department of Physics and Astronomy, BYU
Master of Science

An extensive survey of extragalactic objects with accurate distances is difficult to perform. Distance at that scale is commonly found with redshift and most easily identified with spectroscopic observations, which are time intensive. This is especially a concern when surveying for the elusive, possibly non-existent dwarf galaxies in the centers of voids, whose light would be so faint that a spectroscopic survey to find them would be unreasonably time consuming. Photometric methods to calculate redshift could provide a much quicker way to find distance, but the photometric methods used thus far are characterized by large errors that make them unusable for research on nearby voids. I have been testing two photometric redshift methods that have been recently developed: the Gaussian filter method and the ramp filters method. The Gaussian filter method isolates objects that have emission within the bandpass of the Gaussian filters. Spectroscopic follow-up observations of objects observed with the Gaussian filter method confirmed that 41.9% of the objects identified by the method actually had emission lines within the bandpass of the filters, which is more than a random sampling where only 7% of galaxies had emission within that wavelength range. Assuming that all the lines identified were Hα, the photometric redshift calculated from the Gaussian filter observations had an error of 945 km·s^{-1} (or 430 km·s^{-1} by excluding one outlier). Ramp filter observations of objects with SDSS redshifts provided a way to identify redshift with an error of 641.8 km·s^{-1}. These errors are about an order of magnitude less than other redshift methods. These methods show promise for uses in observational cosmology, specifically extragalactic survey work and searching for void galaxies.

Keywords: observational cosmology, photometric redshift, void galaxies

ACKNOWLEDGMENTS

First, I thank Dr. J. Ward Moody. He has worked with me throughout my undergraduate and graduate degrees and has always been eager to help. He has taught me so much about astronomy and research. He has also taught me that there is more to life than work. I am grateful for his patience and encouragement.

I would also like to thank my husband, Jackson, who has supported me through the ups and downs of this work.

The Digitized Sky Surveys were produced at the Space Telescope Science Institute under U.S. Government grant NAG W-2166. The images of these surveys are based on photographic data obtained using the Oschin Schmidt Telescope on Palomar Mountain and the UK Schmidt Telescope. The plates were processed into the present compressed digital form with the permission of these institutions.

Funding for the Sloan Digital Sky Survey IV has been provided by the Alfred P. Sloan Foundation, the U.S. Department of Energy Office of Science, and the Participating Institutions.

SDSS-IV acknowledges support and resources from the Center for High Performance Computing at the University of Utah. The SDSS website is www.sdss.org.

SDSS-IV is managed by the Astrophysical Research Consortium for the Participating Institutions of the SDSS Collaboration including the Brazilian Participation Group, the Carnegie Institution for Science, Carnegie Mellon University, Center for Astrophysics | Harvard & Smithsonian, the Chilean Participation Group, the French Participation Group, Instituto de Astrofísica de Canarias, The Johns Hopkins University, Kavli Institute for the Physics and Mathematics of the Universe (IPMU) / University of Tokyo, the Korean Participation Group, Lawrence Berkeley National Laboratory, Leibniz Institut für Astrophysik Potsdam (AIP), Max-Planck-Institut für Astronomie (MPIA Heidelberg), Max-Planck-Institut für Astrophysik (MPA Garching), Max-Planck-Institut für Extraterrestrische Physik (MPE), National Astronomical Observatories of China, New Mexico State University, New York University, University of Notre Dame, Observatário Nacional / MCTI, The Ohio State University, Pennsylvania State University, Shanghai Astronomical Observatory, United Kingdom Participation Group, Universidad Nacional Autónoma de México, University of Arizona, University of Colorado Boulder, University of Oxford, University of Portsmouth, University of Utah, University of Virginia, University of Washington, University of Wisconsin, Vanderbilt University, and Yale University.

Contents

List of Figures

List of Tables

Chapter 1

Introduction

1.1 Large Scale Structure and ΛCDM

Observational cosmology is the study of the formation and organization of matter in the Universe on scales much larger than galaxies. From research in this field, we know that galaxies in the Universe coalesce into clusters and groups which then create a web-like network of clusters and filaments collectively known as the "large scale structure" or "LSS". Based on our theoretical understanding of the origins, expansion and make-up of the Universe, this cosmic web has been recreated in simulations such as the Millennium simulation (Springel et al. 2005). The Millennium simulation is in good agreement with observational data from the Sloan Digital Sky survey (SDSS) on a large scale (Nurmi et al. 2013).

Springel et al. (2005) used only dark matter particles in the Millennium run. The impressively high accuracy of the simulation on the large scale indicates that dark matter is a key to the formation of the LSS of the Universe. This reveals the importance of understanding the nature of dark matter. The theory adopted by Springel et al. (2005), and the currently accepted model, is the Λ Cold Dark Matter (ΛCDM) theory. ΛCDM is the most widely accepted theory for dark matter and dark energy.

It stipulates that dark matter, which makes up 84% of the matter in the Universe (Hinshaw et al. 2013), is cold (i.e., has low energy) and that there is a field of dark energy (Λ) that adds a repelling force to the Universe.

The large-scale success of Springel et al. (2005) supports the ΛCDM theory. There are, however, some discrepancies between the theory and observations of the actual Universe, specifically when looking at the smaller scales. These conflicts include the Too-Big-To-Fail problem (Boylan-Kolchin et al. 2011), the missing satellite problem (Klypin et al. 1999; Moore et al. 1999), and the void phenomenon (Peebles 2001). The void phenomenon is the problem that will be investigated further in this paper. I will discuss this phenomenon in more depth in Section 1.3.

1.2 Dark Matter

The cold dark matter described in the current concordance cosmology is not the only theory about the nature of dark matter. It is important to understand these theories to grasp potential solutions to the discrepancies in the ΛCDM model.

While there are many theories about the nature of dark matter, I will describe three in detail: cold dark matter (CDM), warm dark matter (WDM) and hot dark matter (HDM). The temperature of the theoretical dark matter refers to the energy or speed of the dark matter particles. Low mass particles have a lot of kinetic energy and move very quickly which, according to the Maxwell-Boltzmann distribution, usually corresponds to a higher temperature. Thus, if dark matter is made up of high energy, relativistic particles, it would fall under the category of hot dark matter. If instead dark matter particles are high mass, low energy and slow moving, these would be cold dark matter. Specifically, dark matter is considered cold if the energy of movement is negligible. Warm dark matter refers to dark matter particles that fall in between these two categories.

Blumenthal et al. (1984) described how these types of dark matter can affect the formation of galaxies in unique ways. In the early Universe, everything was moving quickly - too quickly for particles to come together gravitationally because their kinetic energy was so great that they would just separate again. As the Universe expanded, the particles lost energy and slowed down. Larger, more massive, particles would slow down first, and the lighter, or less massive, particles remained at higher speeds for longer.

In an HDM dominated universe the lightest particles, like neutrinos, that make up hot dark matter wouldn't slow down enough to start to combine until the particle horizon of the universe, or the part of the universe within which all the particles can interact with each other, was very large and included about $10^{15}M_{\odot}$ of neutrinos. This is about the mass of clusters of galaxies today, so in a HDM dominated universe, the first objects to form would be clusters. These would then break down to form galaxies. This is called top-down formation.

In a CDM dominated universe, the dark matter particles are larger - so large that they slowed down very quickly. These particles reached slow enough velocities to form into halos when the particle horizon encompassed only a small amount of dark matter particles. This group of dark matter particles that will form the first halos are about the size of a dwarf galaxy. This indicates that dwarf galaxies will form first in a CDM dominated universe and then combine to form larger galaxies and clusters. This is called bottom-up formation.

Finally, in a WDM dominated universe the particles that make up most of the dark matter would be more massive than the HDM neutrinos but less massive than CDM particles, so WDM particles would slow down at a rate between HDM and CDM as the universe expanded. These particles would reach a speed slower than relativistic speeds when the particle horizon of the universe contains about $10^{11}M_{\odot}$ of WDM particles. This is about the mass of a regular galaxy, indicating that a WDM dominated universe will preferentially create galaxies first, which will combine into clusters and

break down into smaller galaxies. So a WDM dominated universe is bottom-up for larger galaxies and clusters of galaxies and top-down for creating dwarf galaxies.

The size of the particle horizon when the particles begin to coalesce, also called the free-streaming length (FSL), can be used to identify the difference between cold, warm and hot dark matter. If the FSL is much smaller than a dwarf galaxy, it is CDM. If the FSL is about the same size as a dwarf galaxy, it is WDM. And if the FSL is much larger than a dwarf galaxy, then it is HDM (Umemura & Ikeuchi 1985; Vittorio & Silk 1984).

While the currently most accepted theory is that the majority of dark matter is CDM, it is still possible that the solution to the ΛCDM problems mentioned in Section 1.1 will require us to adjust our view of dark matter.

1.3 Voids

Between the clusters and filaments of galaxies there are pockets of space called “voids” which are empty of regular sized galaxies. ΛCDM predicts that many small dark matter halos should exist there, which would lead to a density of dwarf galaxies about equal to the cosmic mean. This is not, however, what is observed. While galaxies may litter the edges of these voids, no dwarf galaxy has ever been discovered deep within a void.

This stark under-abundance of dwarf galaxies in voids is a problem termed the "void phenomenon" by Peebles (2001). As reported by Tikhonov & Klypin (2009), the CDM model predicts ten times as many dark matter halos as there are dwarf galaxies observed in the voids. This indicates one of two things: either there is a problem with the current theory that needs to be remedied, or the under-abundance of dwarf galaxies is an observational bias.

If the lack of dwarf galaxies in voids is an accurate observation, then there must be something suppressing dwarf galaxy formation in the voids. It is possible this suppression is because the

Universe is dominated by WDM instead of CDM. Bode et al. (2001) showed that WDM leads to a suppression of small halos, which could be applied to the phenomenon seen in voids. With fewer small dark matter halos, fewer dwarf galaxies would be able to form.

Some believe that the lack of dwarf galaxies in voids can be easily explained with baryonic effects and that the CDM model shouldn't be thrown away so quickly. Tinker & Conroy (2009) explain that they were able to simulate the under-dense voids by applying a bias factor. A bias factor is included in models of the LSS to acknowledge that galaxies do not always form where there is a dark matter halo. Simpson et al. (2013) predicted that the suppression of dwarf galaxy formation in the voids could be the result of reionization, supernovae explosions and UV radiation from nearby galaxies pushing baryonic material out of the voids so they could not form into dwarf galaxies.

According to the work of Reed et al. (2015), simulations of the LSS of CDM universes with suppressed dwarf galaxy formation and WDM universes were very similar. It follows that determining between the baryonic affects and WDM being the cause of this supposed under-density will require more research and observations.

This is all, of course, assuming that the disparity between observations and the CDM theory is correct. It is possible that the under-density is a mistake because the process of finding galaxies is inherently biased against finding the faint dwarf galaxies that would reside in voids. This bias is because the method used to find distance, spectroscopic redshift, is inefficient at conducting survey work and observing faint objects, as is discussed further in Section 1.4.

1.4 Redshift

The method that is commonly used to find the distance to astronomical objects on the scale of the LSS is called cosmological redshift. This method is based on the fact that, according to observations, the Universe is expanding (Hubble 1929; Hubble & Humason 1931). This expansion is not simply a

result of galaxies receding from each other; space-time itself, within which everything is embedded, is stretching. As a result, everything in the Universe is pulled apart as well. Light, which is also embedded in space-time, is affected by this expansion. Traveling light waves are stretched by the cosmological expansion, giving the light a longer wavelength, and therefore redder color, than it originally had. The value of the redshift, represented by z, is found by

$$z = \frac{\lambda - \lambda_o}{\lambda_o}, \tag{1.1}$$

where λ is the observed wavelength and λ_o is the original wavelength of the light when it was emitted by the source.

This redshift can be used to find the distance to the source galaxy. When $z \leq 2$, that relationship is approximately

$$d \approx \frac{c}{H_0} \frac{(z+1)^2 - 1}{(z+1)^2 + 1}. \tag{1.2}$$

When $z << 1$, this simplifies to

$$d = \frac{cz}{H_0}. \tag{1.3}$$

For both Equation 1.2 and 1.3, d is distance to the galaxy in Mpc, c is the speed of light in km·s^{-1}, z is redshift and H_0 is the Hubble constant. The exact value of the Hubble constant is debated, but for this work I will assume a value of $H_0 = 70$ km·s^{-1}· Mpc^{-1}. The product of the speed of light and the redshift, cz, is an important value in cosmology often casually referred to as the redshift.

The most common method to observe redshift is spectroscopy, where you use the spectrum or spectral energy distribution (SED) of an object, obtained by splitting the light with a grating to separate it by wavelength. Figure 1.1 gives a typical spectrum of an emission line galaxy, where the light of the galaxy is dominated by emission lines from gas rather than a blackbody continuum from stars. To calculate redshift from a spectrum like this, one simply needs to find a known feature, like

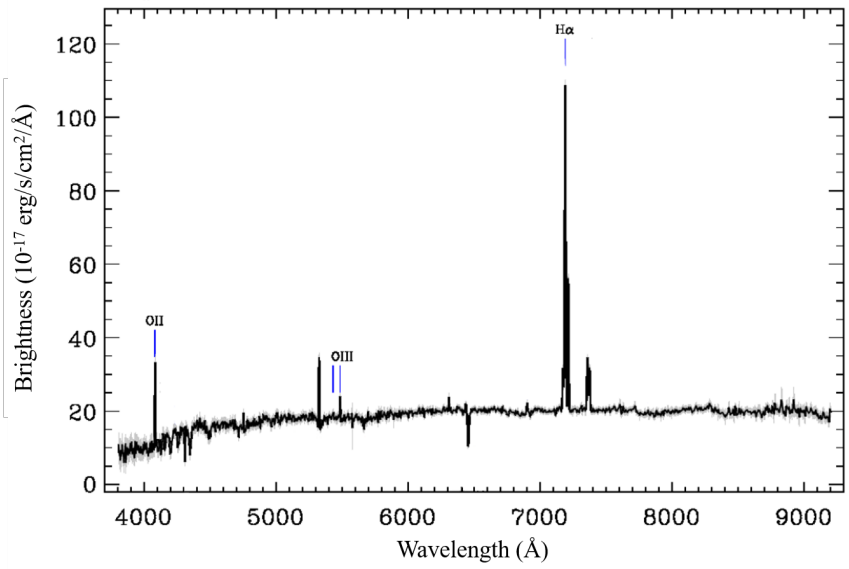

Figure 1.1 The spectrum of a typical emission line galaxy. The x-axis is the wavelength in Angstroms and the y-axis is the flux or brightness of the galaxy at that wavelength. Adapted from Abolfathi et al. (2018).

the Hα emission line, identify how much it has been shifted from the original wavelength, and use Equation 1.1 to find the redshift. In this instance, the rest wavelength of the Hα emission line is λ_o = 6563Å, but the spectrum in Figure 1.1 has the Hα line at about λ = 7200Å. Using Equation 1.1, the value that comes out for redshift is $z = 0.097$ or $cz = 2.91 \times 10^4 \text{km}\cdot\text{s}^{-1}$, from multiplying by the speed of light, $c = 2.998 \times 10^5 \text{km}\cdot\text{s}^{-1}$.

Spectroscopy provides a straightforward method to determine redshift, but it has some drawbacks. It is time consuming to take spectroscopic data, because it is performed on a limited number of objects at a time. Spectroscopy also requires a lot of light from the object being observed, meaning it requires a longer exposure time and cannot be done on objects that are too faint. Because of these complications with spectroscopy, it is inefficient to use for survey work and biased against finding faint galaxies.

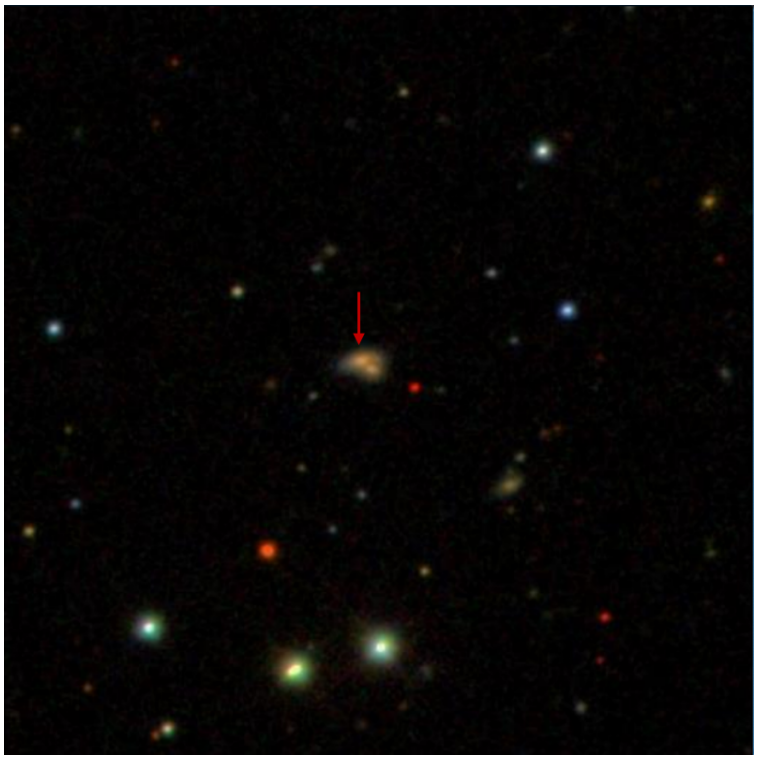

Figure 1.2 A photometric image of the same galaxy shown spectroscopically in Fig 1.1. The red arrow indicates the galaxy. Adapted from Abolfathi et al. (2018)

.

It would be ideal to use a quicker method to find redshift. Some have attempted this using photometry rather than spectroscopy. Photometry is a method of observing astronomical objects where, instead of splitting the light by wavelength and getting a spectrum, you observe in one band-pass filter at a time. You can combine multiple images to make a multi-color image, like Figure 1.2. Figure 1.2 shows the same galaxy from Figure 1.1 as it looks in a photometric image.

Many objects can be photometrically observed at once – as many as will fit in a frame. It also doesn't require as much light as spectroscopy because the observed flux is not split up by wavelength but combined into one measurement. While photometry may be superior to spectroscopy in ease of observations, it does not gather as much information as spectroscopy does. With a spectrum, there is much about an astronomical object you can learn such as temperature, metallicity and

distance. With photometry, all you learn is how much flux there is in a certain band-pass filter, and the observer must get creative to determine more from that.

There are many who have developed methods to find redshift photometrically, but these attempts have led to results far less accurate than those provided by spectroscopic observations. Some of these methods, with their successes and their setbacks, are described in Section 1.5.

1.5 History of Photometric Redshift

Baum (1962) published the first photometric redshifts. He worked with galaxies from a number of clusters. He chose the brightest two to six galaxies in each cluster, observed them in multiple filters and took the average value between these galaxies for each filter. He then plotted those average values by wavelength to get a crude estimate of the SED. Fitting those values to the model he created from doing the same measurements on the nearby Virgo cluster, he measured how far the fit had shifted from where it was originally to calculate the redshift, assuming that the SED of the Virgo cluster accurately modeled the SED of the distant galaxy if it had a redshift of z = 0. The probable error of cz calculated by this method was highly dependent on the distance to the cluster being observed and ranged from 57 to 9400km·s^{-1}.

There are many who have followed Baum with their own techniques. Connolly et al. (1995) observed galaxies in four filters (U, B_J, R_F, and I_N) and found that a galaxy's placement in the four-dimensional space defined by those measurements was related to the redshift, spectral type and luminosity for that galaxy. They were able to simplify it in a way to single out redshift and found a photometric redshift as accurate as $\Delta cz = 6000$km·s^{-1}.

Another method, published by Bolzonella et al. (2000), took measurements in broadband filters and computationally identified which of many galaxy templates would be the best fit, fit it to the data and measured the redshift according to that template. Their accuracy was $\sigma_{cz} = 9000$km·s^{-1}.

Collister & Lahav (2004) wrote an artificial neural network to find a relationship between photometric measurements and redshift and tested it on SDSS data with an accuracy of $\sigma_{cz} = 6900\text{km}\cdot\text{s}^{-1}$.

Given the accuracy of these and other methods from the almost 60 years following Baum's work, some of the low errors he calculated, especially considering the simplicity of the method, seem almost to good to be true. Because of this, I will use the combined errors of the many subsequent methods to estimate the average accuracy of modern photometric redshift methods. By this standard, current photometric methods seem to have an accuracy of about 6000 to $9000\text{km}\cdot\text{s}^{-1}$. This uncertainty spans the size of the structures I am trying to probe, namely galactic voids, so more accurate methods are needed to have any hope of using photometric redshift to survey for void galaxies in the Universe with any confidence.

1.6 New Methods of Photometric Redshift

There are two recently developed techniques for calculating photometric redshift that I used in this research. I will describe them in the subsections below.

1.6.1 Gaussian Filters

One of these techniques uses Gaussian shaped photometric filters, as described in Draper (2019). A schematic of these filters, from Steele (2019), is given in Figure 1.3. This figure depicts the percentage of signal transmitted through the filters at each wavelength. This method used three narrow filters with wings that give them a rough Gaussian shape, which I refer to as "Gaussian filters", seen in Figure 1.3: The Hα8 filter, shown in blue in the figure, the Hα12 filter, in red, and the Hα16, in yellow. These filters are named based on the redshift expected for the Hα line to fall

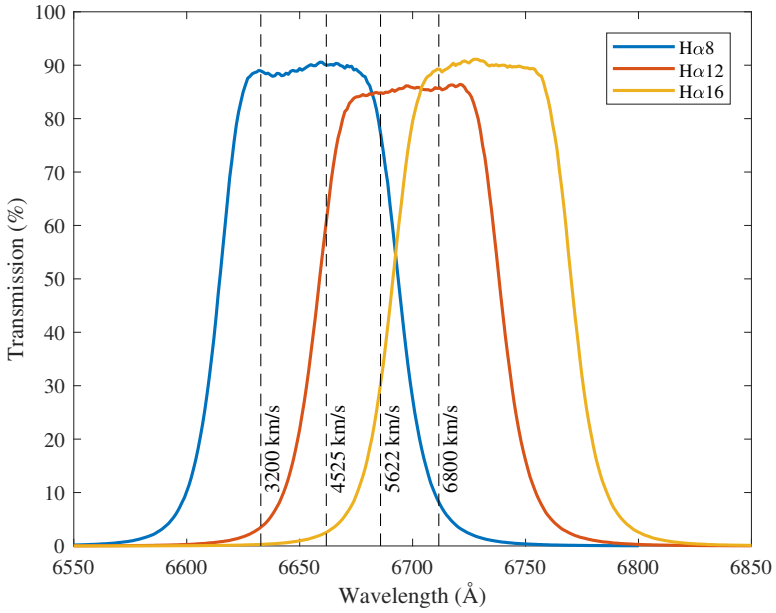

Figure 1.3 A schematic of the transmission of the Gaussian filters over the wavelengths of the bandpass. The Hα8 filter is shown in blue, Hα12 in red and Hα16 in yellow. The dashed lined marked by redshift (cz) values in km·s^{-1} are identifying where the Hα emission line would be for a galaxy at the redshift noted. So a galaxy with a redshift of 3200km·s^{-1} would have an Hα emission line at the first dashed line on the left. Figure from Steele (2019).

in the center of that filter. The Hα8 filter is centered around an Hα line that has been redshifted by 8nm, and the other two filters follow the same rule.

This method utilizes the wide wings of the filters to determine where within the bandpass the Hα emission line is. With multiple filters, the signal within each can be compared to identify the precise location of the line.

Suppose an emission line galaxy with a redshift of 4525km·s^{-1} is observed with this filterset. The Hα emission line would fall at the dashed line labeled 4525km·s^{-1} on Figure 1.3. Because most of the light from these small emission line galaxies is from the emission line, and the filters are narrow, we can assume the light from the continuum is negligible. This means that, with the Hα line at the 4525km·s^{-1} dashed line, the Hα8 filter will capture about 90% of the light from the

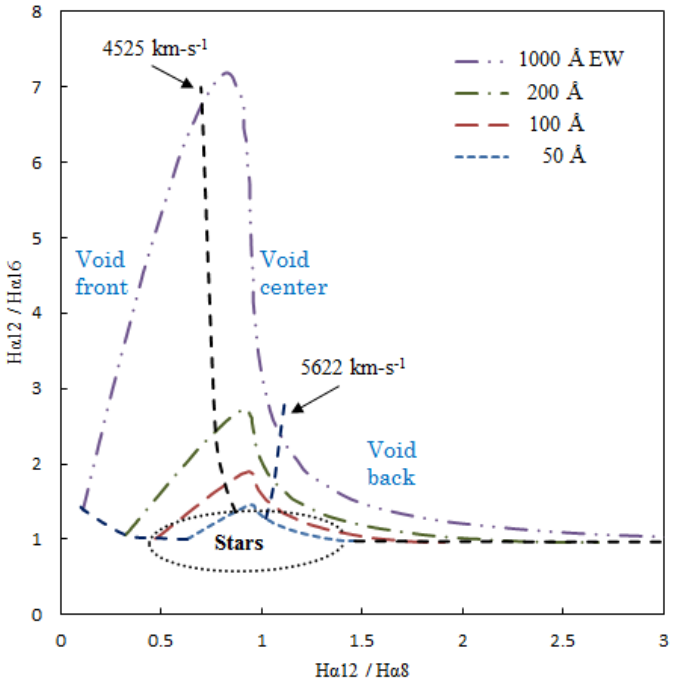

Figure 1.4 Mapping to redshift and EW from the ratios Hα12/Hα8 and Hα12/Hα16. Redshift identified on black dashed lines. Equivalent width shown on the colored lines. From Draper et al. (in prep).

emission line (and therefore 90% of the total light from the galaxy). The Hα12 filter will capture about 60% of the light and the Hα16 filter will capture about 2% of the light. The resulting ratios of the flux from these filters, specifically Hα12/Hα8 and Hα12/Hα16, can be mapped to a unique redshift and equivalent width (EW).

This mapping is shown in Figure 1.4. This figure shows how the EW and redshift of an object can be determined from the Hα12/Hα8 and Hα12/Hα16 ratios, depicted on the x and y axes, respectively. The various redshift values are shown by the black dashed lines and the EW values are the colored dashed and dotted lines. Based on this figure, redshift increases moving to the right around the curve and equivalent width increases moving up.

Both of the above methods assume that the emission line captured in the bandpass of these filters is the Hα line. It is possible, and very common, for a galaxy to reside behind the void at such

a distance that a different emission line is observed. The two emission lines that cause concern are the [OIII]$\lambda\lambda$5007, 4959Å doublet (hereafter [OIII]) and the [OII]λ3727Å blended line (hereafter [OII]). Since galaxies with [OIII] and [OII] can easily contaminate the field, it is important to be able to distinguish which lines are Hα, [OIII] and [OII]. This can be done by observing the galaxy as a whole through broadband filters.

Whether the emission observed is Hα, [OIII] or [OII] tells us the distance to the galaxy emitting the light. This distance indicates how far back in time these observations are going.

Figure 1.5, from Draper (2019), compares the Hα, [OIII] and [OII] groups of galaxies. The figure shows the unique populations that are apparent when comparing the color indices of the Sloan broadband filters, specifically g'-r' and r'-i'. Each point on this figure is one of 827 galaxies from the SDSS survey. The red points represent 648 galaxies with a redshift of cz = 1,600km·s^{-1} to 9,400km·s^{-1}, which would make the Hα line detectable in the narrowband filters. The green points are the 20 galaxies at a redshift of z = 0.32 to 0.35, with [OIII] emission captured in the narrowband filters. And the blue points are the 159 galaxies at a redshift of z = 0.77 to 0.82, with [OII] emission observed in the narrowband filters. The three groups of galaxies appear to occupy three distinct areas on the graph, with a fair amount of overlap.

The inner dashed circle indicates the region within which 1σ of the Hα galaxies are located and the outer dash-dotted circle is the region where 2σ of the Hα galaxies are located. The area to the lower left of these circle is almost entirely populated by Hα galaxies, and as such is referred to as the Hα region. Inside the 2σ region, 78.4% of the object are Hα, 2.4% are [OIII] and 19.2% are [OII]. The objects in the 1σ region are 91.9% Hα, 0.2% [OIII] and 7.9% [OII].

Using a combination of the narrowband and broadband filters and methods, this technique calculates the redshift of each object. This method is still being tested and confirmed with spectroscopy as part of this thesis.

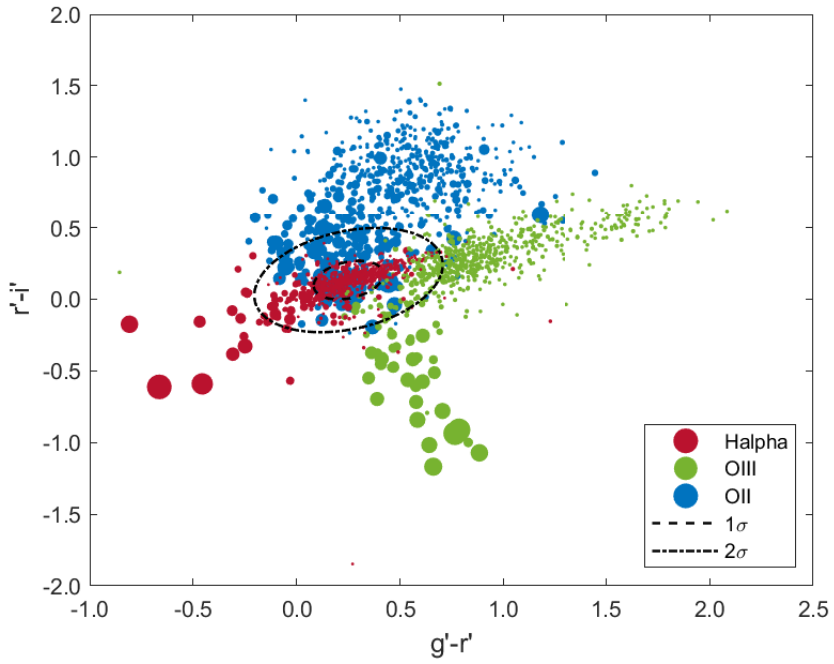

Figure 1.5 This figure plots the color indices $g' - r'$ and $r' - i'$ of three groups of galaxies, each at a different distance to put different emission lines within the bandpass of the Gaussian filters, Hα, [OIII] and [OII]. The size of each point is proportional to the equivalent width of the emission line of the galaxy. The scale is normalized to keep the point sizes similar between galaxy populations. The dashed ellipse contains 1σ of the Hα galaxies in the sample. Within this region, 91.9% of the objects are Hα, 0.2% are [OIII] and 7.9% are [OII]. The dashed-dotted ellipse contains 2σ of the Hα galaxies. Within this region, 78.4% of the objects are Hα, 2.4% are [OIII] and 19.2% are [OII]. From Draper (2019).

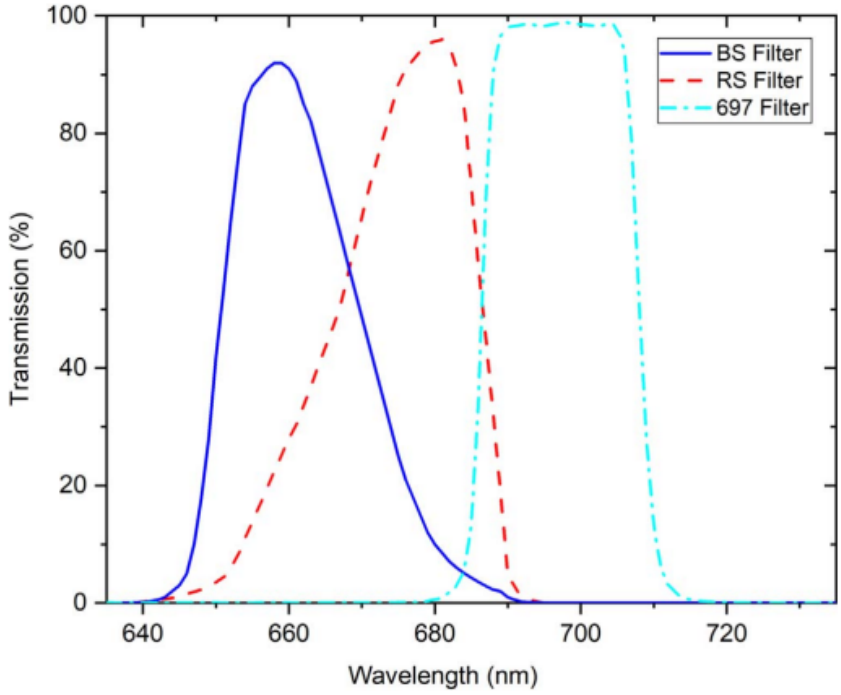

Figure 1.6 A schematic of the ramp filters from Lesser et al. (2019).

1.6.2 Ramp Filters

Another recent technique for finding photometric redshift was introduced in Lesser et al. (2019). In this work, they used asymmetric bandpass filters, called ramp filters, with a transmission shown in Figure 1.6. The x-axis of the figure represents the wavelength being observed and the y-axis represents the percentage of light allowed through the filter at that wavelength, or the transmission. Each filter is represented by a different colored line. The solid blue line represents the blue sloping or BS filter, the dashed red line is the red sloping or RS filter and the dot-dashed light blue line represents the 697 filter, which will be referred to as the continuum filter in the rest of this paper.

These ramp filters introduced in Lesser et al. (2019) should not be confused with the ramp filters used by the Advanced Camera for Surveys (ACS) and the Wide Field and Planetary Camera 2 (WFPC2) on the Hubble Space Telescope (HST). The filters used on the ACS and the WFPC2 termed ramp filters are narrow- to medium- band filters that can be tuned to the desired wavelength

when observing spectral features. The filters referred to in this paper are broadband filters named for their sloping wings and are not tunable.

The blue and red sloping ramp filters are designed to capture within their band-pass the Hα emission line with a redshift of $0 < cz < 12,000\text{km}\cdot\text{s}^{-1}$. With the H$\alpha$ emission line in the band-pass, the measurements from the ramp filters can be used to determine the exact redshift of the galaxy being observed.

As an example of how the method from Lesser et al. (2019) works, imagine observing a strong Hα emitting galaxy which is redshifted so the Hα line is at about 660nm. In other words, the galaxy is very bright at 660nm and relatively dim at all the other wavelengths within the bandpass of the ramp filters. In this case, a large percentage of the bright emission line will be observed in the BS filter because at 660nm, the BS filter has a transmission of about 80%. A smaller portion of the emission line will be observed in the RS filter, which only has a transmission of about 25% at 660nm. The total brightness in the BS filter will be brighter than that in the RS filter, so the ratio of BS/RS will be greater than 1.

Now, suppose there is another galaxy observed that is more distant so that the Hα line has been redshifted to about 680nm. In this case, the BS filter will only observe about 10% of the light from the emission line while the RS filter will observe about 95% of the light, making the observation in the RS filter much stronger than that in the BS filter, so the ratio BS/RS will be less than 1.

Once the relationship between the BS/RS ratio and the redshift of a galaxy is known, then by observing any galaxy with Hα emission within the redshift range with the BS and RS filters and calculating the ratio of the two, one can evaluate the redshift of that galaxy.

This method works under the assumption that all the light observed in the BS and RS filters comes from the emission line, which is not quite true. Every galaxy has an underlying continuum that comes from stars and other black-body radiation. The continuum filter in Figure 1.6 is used to identify and then subtract out that continuum. The continuum filter is designed to avoid major

emission lines, so that all the light in the continuum filter should be from the continuum. If one assumes the continuum is flat, which is close to true when observing a small range of wavelengths, and since the width of the filter is known, the continuum itself can be estimated within the continuum filter. By assuming the continuum in the ramp filters is about the same as the continuum in the continuum filter, the calculated continuum can then be subtracted from the measurements in the ramp filters, leaving only the light from the emission line.

In Lesser et al. (2019), they calculated a relationship between the redshift and the BS/RS ratio and found that the ramp filter method could predict the redshift of a galaxy with an accuracy of $\Delta cz = 573\text{km}\cdot\text{s}^{-1}$. That is an order of magnitude improvement over other photometric methods.

One issue Lesser et al. (2019) came across in their research is that other emission lines, even small ones, around the Hα line can disrupt the calculations - specifically, the [SII]$\lambda\lambda$6716,6731Å doublet (hereafter [SII]), which is an emission feature that falls just to the red side of Hα. For galaxies with a redshift z < 0.018, the [SII] line falls within the bandpass of the RS filter, making the Hα emission seem brighter than it is in that filter. At a redshift of about z = 0.018, the [SII] line shifts from the RS filter to the continuum filter, so at redshifts of z > 0.018, the continuum gets over-estimated with the presence of the [SII] line in the continuum filter. This produces a bump in the RS/BS relationship, which increases the error. The presence and magnitude of the so-called "[SII] bump" is one aspect of the ramp filters method that will be addressed in this work. In my master's research I will fine-tune and improve the ramp filter method so that it can one day be accessible to other researchers studying the LSS of the Universe.

Chapter 2

Gaussian Filters Technique

2.1 Spectral Confirmation Methods

To confirm the Gaussian Filter method described in Section 1.6.1, candidate void galaxies identified by the method must be observed spectroscopically to determine the redshift with this more conventional method. These spectroscopic observations were made using the Astrophysical Research Consortium (ARC) 3.5m telescope at Apache Point Observatory (APO) on the Dual Imaging Spectrograph (DIS). There were two gratings used, one for the red spectrum and one for the blue. The grating used for the red spectrum was the R300 grating which offered a wavelength coverage of 5190Å to 9810Å and a linear dispersion of 2.31Å/pixel. The blue grating was the B400 grating, with a wavelength coverage of 2570Å to 6230Å and a linear dispersion of 1.83Å/pixel. A 2.0" slit was used for the observations.

Targets were chosen from candidates in the second and eighth voids indexed in Foster & Nelson (2009), hereafter FN2 and FN8. To be chosen, the candidates needed to fall within the 1σ, 2σ or Hα region of Figure 1.5 and have a magnitude brighter than 21. Priority was also given to objects with a stronger emission line as estimated by the narrowband filters. A list of the targets observed is

given in Table 2.1. All of the objects listed in Table 2.1 except one, FN8-45-16341, fall into just one of the sections in the GRI color-color plot, as listed in column 6. FN8-45-16341 is one of seven objects in Draper (2019) that fell into both the Hα and 2σ regions.

Table 2.1 Target objects observed with ARC. The first two columns give the field the object is in and the identification number. The next two columns give the RA and declination of the object. Column five is the magnitude of the object in the r′ filter. The sixth column gives the section the object falls within in the GRI broadband plot, Figure 1.5, and the seventh column is the date observed in UTC.

Field	ID	RA (J2000.0)	Dec (J2000.0)	Magnitude (r′)	Hα section	Obs date (UTC)
FN2-22	4803	$03^h41^m33^s.98$	$17°45'55''.6$	19.8	2σ	1/12/21
FN2-22	6323	$03^h42^m18^s.83$	$17°51'32''.1$	19.7	2σ	1/12/21
FN2-22	6936	$03^h42^m30^s.20$	$17°54'16''.7$	20.2	2σ	2/6/21
FN2-22	7633	$03^h41^m42^s.61$	$17°57'07''.3$	20.3	2σ	2/6/21
FN2-22	8150	$03^h42^m34^s.04$	$17°59'23''.8$	19.9	2σ	1/12/21
FN2-22	9134	$03^h42^m11^s.24$	$18°03'24''.0$	20.0	2σ	2/6/21
FN2-22	9164	$03^h41^m10^s.62$	$18°03'25''.8$	20.4	1σ	11/14/20
FN2-22	11932	$03^h41^m21^s.03$	$18°13'57''.1$	20.2	1σ	2/6/21
FN2-23	4526	$03^h41^m32^s.64$	$17°08'20''.4$	20.0	2σ	2/6/21
FN2-23	7035	$03^h41^m49^s.70$	$17°17'06''.4$	20.0	2σ	2/6/21
FN2-23	7179	$03^h42^m56^s.20$	$17°17'39''.8$	18.5	2σ	1/12/21
FN2-23	7651	$03^h41^m28^s.50$	$17°19'18''.9$	19.7	2σ	1/12/21
FN2-23	8674	$03^h41^m49^s.45$	$17°23'07''.4$	19.3	2σ	1/12/21
FN2-32	5251	$03^h44^m00^s.88$	$17°50'13''.1$	21.1	1σ	11/14/20
FN2-32	10088	$03^h44^m33^s.47$	$18°06'50''.3$	19.4	2σ	1/12/21
FN2-33	6064	$03^h45^m37^s.65$	$17°14'58''.4$	19.4	1σ	11/14/20

Table 2.1 ***cont.***

Field	ID	RA (J2000.0)	Dec (J2000.0)	Magnitude (r′)	Hα section	Obs date (UTC)
FN8-34	4185	$12^h32^m44^s.66$	$72°25'57''.6$	20.6	1σ	2/12/21
FN8-34	6530	$12^h31^m07^s.85$	$72°31'25''.9$	19.6	2σ	2/12/21
FN8-34	8185	$12^h31^m43^s.22$	$72°34'50''.8$	19.7	2σ	2/12/21
FN8-34	10395	$12^h33^m10^s.67$	$72°39'42''.8$	19.2	2σ	1/12/21
FN8-34	11439	$12^h33^m39^s.44$	$72°42'14''.7$	20.8	2σ	2/12/21
FN8-34	15362	$12^h26^m28^s.39$	$72°50'42''.8$	20.8	2σ	2/12/21
FN8-43	12351	$12^h42^m18^s.21$	$73°23'51''.8$	20.8	2σ	2/12/21
FN8-45	2887	$12^h40^m13^s.79$	$71°44'00''.4$	19.5	2σ	1/12/21
FN8-45	6206	$12^h42^m43^s.45$	$71°53'40''.4$	18.5	Hα	11/14/20
FN8-45	7617	$12^h42^m17^s.00$	$71°57'15''.9$	19.6	2σ	2/12/21
FN8-45	11878	$12^h36^m59^s.15$	$72°08'02''.4$	16.4	2σ	1/12/21
FN8-45	16341	$12^h41^m14^s.50$	$72°17'55''.2$	16.1	Hα and 2σ	1/12/21
FN8-53	4906	$12^h48^m52^s.31$	$73°06'19''.6$	21.8	Hα	11/14/20
FN8-53	15443	$12^h53^m00^s.38$	$73°27'42''.5$	20.2	2σ	2/12/21
FN8-53	16430	$12^h52^m21^s.03$	$73°30'00''.3$	20.6	2σ	2/12/21

The observations on the ARC telescope took place the nights of November 14, 2020, January 12, 2021, February 6, 2021 and February 12, 2021 (all dates are UTC time and date). For these observations, exposure time varied based on the magnitude of the object. Wavelength calibration frames were taken with HeNeAr lamps.

The images were processed with standard IRAF reductions for long slit spectroscopy. An overscan region was used in place of bias frames, and because of the low dark current (about 1

electron/pixel/hour for the blue chip and 2.7 electrons/pixel/hour on the red chip), dark frames were deemed unnecessary for this work. Flat fields were also not used.

With the fully processed spectra, I was able to accurately identify emission lines. For less common lines I referred to Ralchenko et al. (2010) for an extensive, but not exhaustive, list of emission lines historical observed in galaxies. I definitively determined for each object if, as expected, there was an emission line within the bandpass of the Gaussian filters, between 6600Å and 6770Å, and what that emission line was. With the emission lines identified, I calculated the redshift of each object to determine if it was within the void.

To find the error in the redshift calculations, I calculated the redshift based on other identified emission lines. In this work, I give both the maximum of those calculated errors and the mean of those measurements and identify for each object which is which. When those two values are the same (i.e., there is only one other emission line), I present them as a single error.

2.2 Results and Discussion

I observed 31 objects spectroscopically. These objects were identified as void galaxy candidates by the Gaussian Filter method described in Section 1.6.1. I found that one "object" (3.2%) was not visible at all, 13 objects (41.9%) had no emission, 4 objects (12.9%) had emission outside the band pass and 13 objects (41.9%) had emission within the bandpass, as predicted. Of the 13 objects with emission inside the bandpass, for 1 object (7.7%) that emission was [OII] emission, for 6 objects (46%) it was [OIII] emission, for 1 object (7.7%) it was Hβ emission, for 1 object (7.7%) it was Hγ emission and for 3 objects (23%) it was Hα emission, while 1 object (7.7%) had emission that could not be identified. This is summarized in Table 2.2.

The 3 objects with Hα emission in the bandpass (23% of objects with emission in the bandpass) seem, at first, like they could be within the void, based on the presence of the Hα line within the

No Object					1	3.2%
FN2-23-7035						
No Emission					13	41.9%
FN2-32-10088	FN8-45-16341	FN2-22-11932	FN2-33-6064	FN2-22-8150		
FN2-22-6323	FN8-45-11878	FN2-22-6936	FN2-32-5251	FN2-22-9164		
FN2-22-4803	FN8-45-2887	FN2-23-4526				
Emission Outside Bandpass					4	12.9%
Hα	**[OIII]**	**Hβ**	**[OII]**	**Unclear**		
FN2-22-9134				FN2-23-7651		
FN2-23-8674				FN2-22-7633		
2	0	0	0	2		
50%	0%	0%	0%	50%		
Emission Inside Bandpass					13	41.9%
Hα	**[OIII]**	**Hβ**	**[OII]**	**Unclear**		
FN8-45-7617	FN8-34-10395	FN8-34-6530	FN8-53-4906	FN8-34-4185		
FN8-45-6206	FN8-53-16430					
FN2-23-7179	FN8-34-11439	**Hγ**				
	FN8-43-12351	FN8-53-15443				
	FN8-34-8185					
	FN8-34-15362					
3	6	1 / 1	1	1		
23%	46%	7.7% / 7.7%	7.7%	7.7%		

Table 2.2 A summary of all the objects observed with ARC. Each object falls in the category of "No Object" (nothing visible), "No Emission" (object, but not emission, visible), "Emission Outside Bandpass" (emission was present outside the bandpass of the Gaussian filters) or "Emission Inside Bandpass" (emission was present inside the bandpass of the Gaussian filters). The total number of objects and percentage within these categories are given on the right. Within the categories with emission, objects are sorted based on the identification of the type of emission (Hα, [OIII], Hβ, Hγ, [OII] or unknown emission). The number and percentage of these are given below each column.

bandpass of the Gaussian filters. However, for two of the objects, FN8-45-7617 and FN8-45-6206, these emission lines are redshifted enough that both objects fall just behind the void in question, FN8. The third object, FN2-23-7179, has such a small redshift that it is well in front of the void FN2. This means that no objects were found inside either of the voids FN2 or FN8.

The 9 objects (69.2% of objects with emission in the bandpass) identified with [OII], Hβ, Hγ or [OIII] emission are background objects far behind the void. These types of objects are expected to contaminate the field.

The 18 objects (58.1% of total objects) with no emission within the bandpass of the Gaussian filters were erroneously identified with emission based on the method. This indicates that there may be an issue in the method that must be investigated.

In the work of Draper (2019), redshifts were calculated for objects observed with the Gaussian filters, assuming that the emission line caught in the bandpass of the filters was Hα. While this was only true for three of the objects observed at APO, I calculated what the redshift would be if the twelve objects with emission in the bandpass were Hα galaxies. This is not the actual redshift for these galaxies (except the three mentioned above), but gives us a way to quantitatively evaluate the accuracy of the photometric redshifts against the spectroscopic redshifts gathered for this project.

The photometric and spectroscopic redshifts for the relevant objects are given in Table 2.3. The photometric redshifts are from Draper (2019). The objects with "..." entries for the photometric redshift had too high of an error to accurately estimate the redshift with the Gaussian filter method. The spectroscopic redshift used for object FN8-45-6206 was calculated from the knot (FN8-45-6206-k) because the original coordinates for FN8-45-6206 point to the knot, not the nucleus.

Using the nine objects with valid photometric and spectroscopic redshifts, the error of the photometric redshift as measured by the Gaussian filters is 945 km$\cdot$s^{-1}.

Object FN2-23-7179 has a very small redshift as measured spectroscopically, and the difference between the spectroscopic and photometric redshifts is extreme, five times greater than the next

Object ID	Photometric Redshift ($km \cdot s^{-1}$)	Spectroscopic Redshift ($km \cdot s^{-1}$)
FN2-23-7179	5100	35.8
FN8-34-10395	6100	6769
FN8-34-11439	4500	4536
FN8-34-15362	5800	6932
FN8-34-4185	...	6969
FN8-34-6530	4200	3892
FN8-34-8185	4200	3791
FN8-43-12351	4400	4708
FN8-45-6206-k	...	7085
FN8-45-7617	...	6997
FN8-53-16430	5300	4991
FN8-53-4906	6100	6369

Table 2.3 Photometric and spectroscopic redshifts of objects with emission inside the bandpass of the Gaussian filters. The photometric redshifts were calculated with Gaussian filter observations from Draper (2019). The spectroscopic redshifts were calculated with observations secured at APO for this project.

highest difference. There is no reason to exclude this data point, but it is such an outlier that it is worth noting that without FN2-23-7179, the error is only 430 $km \cdot s^{-1}$.

These relatively low errors show that if the emission line can be correctly identified, the redshift can be calculated with observations from the Gaussian filters.

In the sections below, I will present each of the 31 objects observed with their spectra and a catalog of their observed emission lines, if applicable. They are organized based on whether or not they have emission and if that emission is within the bandpass of the Gaussian filters.

2.2.1 "Objects" with no object

FN2-23-7035

Despite being identified as an emission line object with the Gaussian method, no object was observed in the red or blue images for FN2-23-7035. This could indicate there is an issue with the method, or that the object is fainter than expected.

2.2.2 Objects with no emission

All the objects in this section have no emission visible in their spectra. There are many possible reasons why the Gaussian filter method returned that these objects had emission lines when they do not appear in spectral observations. A night with poor seeing and intermittent cloud cover could have made observations in some filters artificially dimmer than they should have been so that, when compared to observations in other filters, taken without as much cloud cover, it imitated what an emission line would look like - a brightness in certain filters, but not all of them. These spectral observations helped quantify how common this error is in the method.

FN2-22-9164

Figures 2.1a and 2.1b show the blue and red spectra of FN2-22-9164, respectively.

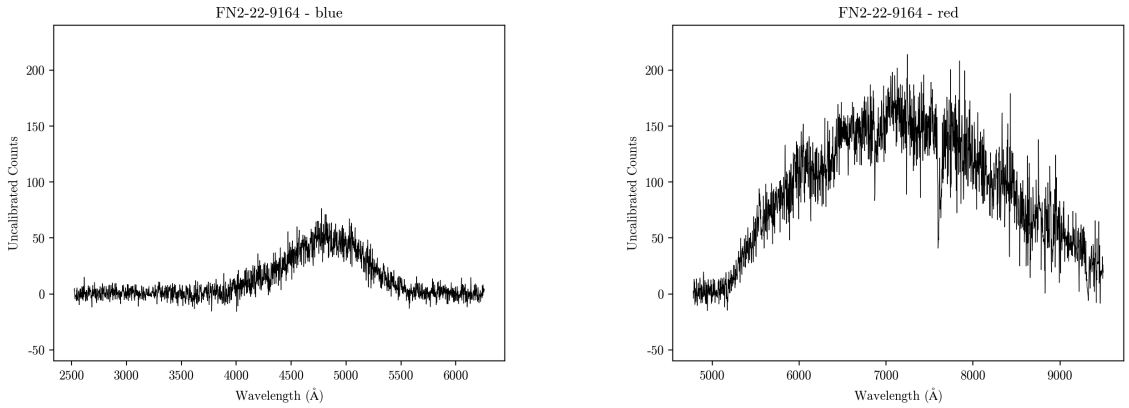

(a) Blue spectrum of FN2-22-9164. **(b)** Red spectrum of FN2-22-9164.

Figure 2.1 Blue and red spectra for FN2-22-9164.

FN2-33-6064

Figures 2.2a and 2.2b show the blue and red spectra of FN2-33-6064, respectively.

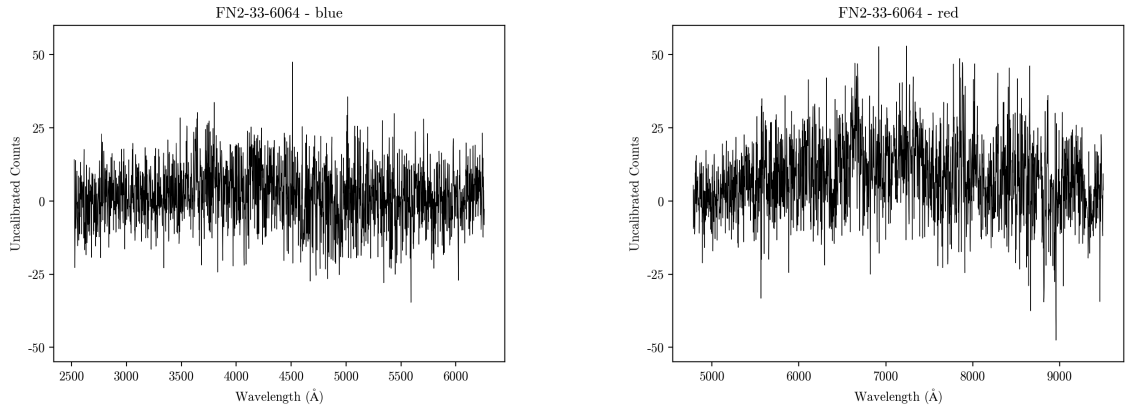

(a) Blue spectrum of FN2-33-6064. **(b)** Red spectrum of FN2-33-6064.

Figure 2.2 Blue and red spectra for FN2-33-6064.

FN2-32-10088

Figures 2.3a and 2.3b show the blue and red spectra of FN2-32-10088, respectively.

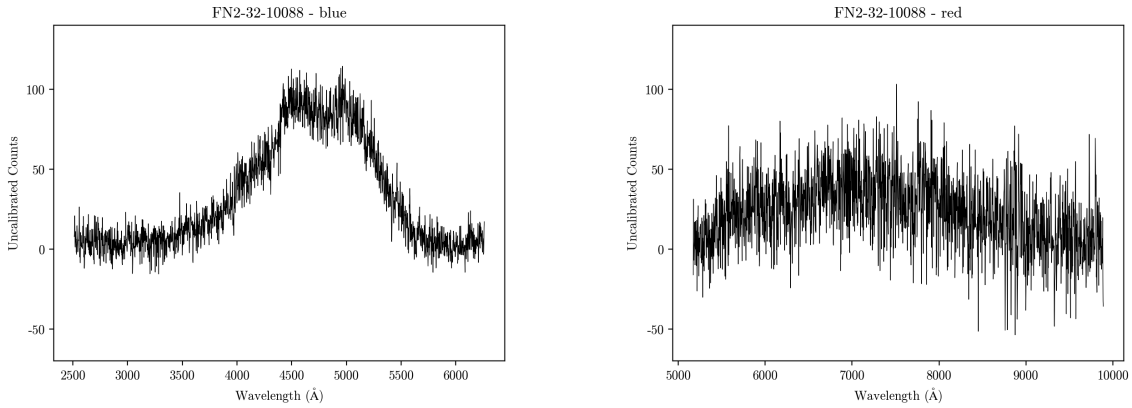

(a) Blue spectrum of FN2-32-10088. **(b)** Red spectrum of FN2-32-10088.

Figure 2.3 Blue and red spectra for FN2-32-10088.

FN2-22-6323

Figures 2.4a and 2.4b show the blue and red spectra of FN2-22-6323, respectively.

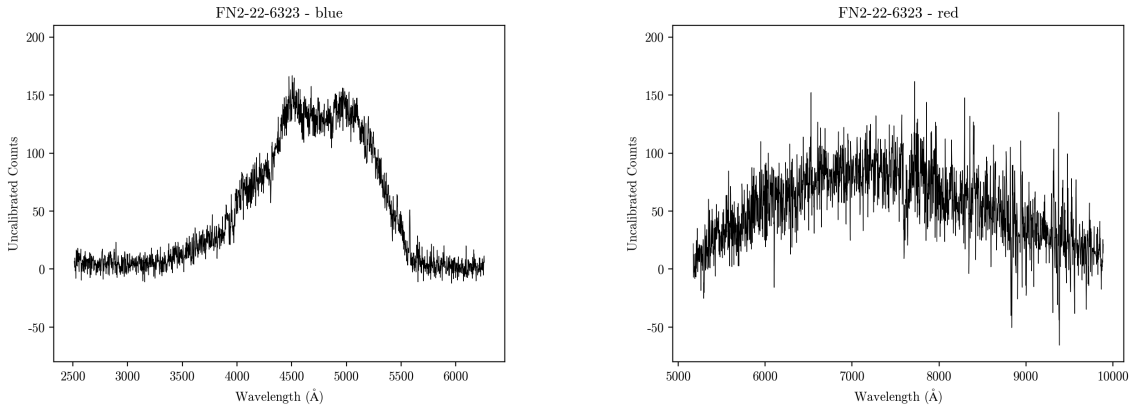

(a) Blue spectrum of FN2-22-6323. **(b)** Red spectrum of FN2-22-6323.

Figure 2.4 Blue and red spectra for FN2-22-6323.

FN2-22-4803

Figures 2.5a and 2.5b show the blue and red spectra of FN2-22-4803, respectively.

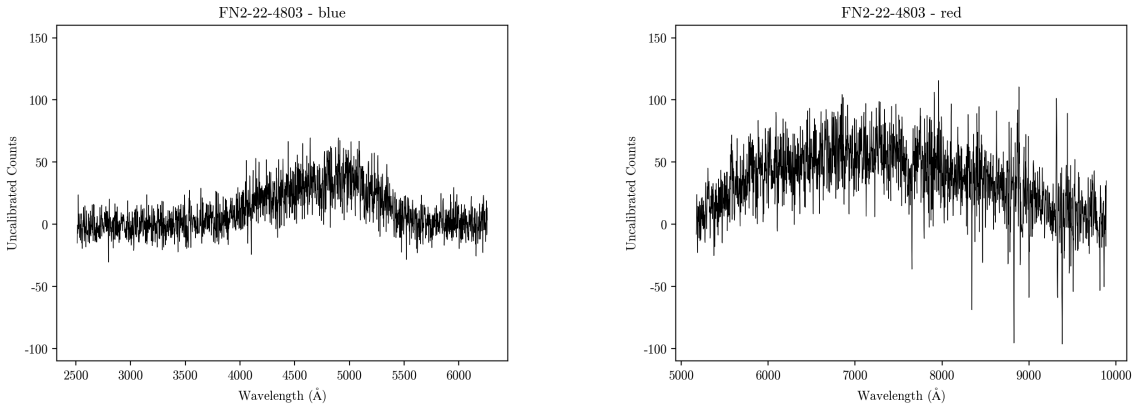

(a) Blue spectrum of FN2-22-4803. **(b)** Red spectrum of FN2-22-4803.

Figure 2.5 Blue and red spectra for FN2-22-4803.

FN2-22-8150

Figures 2.6a and 2.6b show the blue and red spectra of FN2-22-8150, respectively.

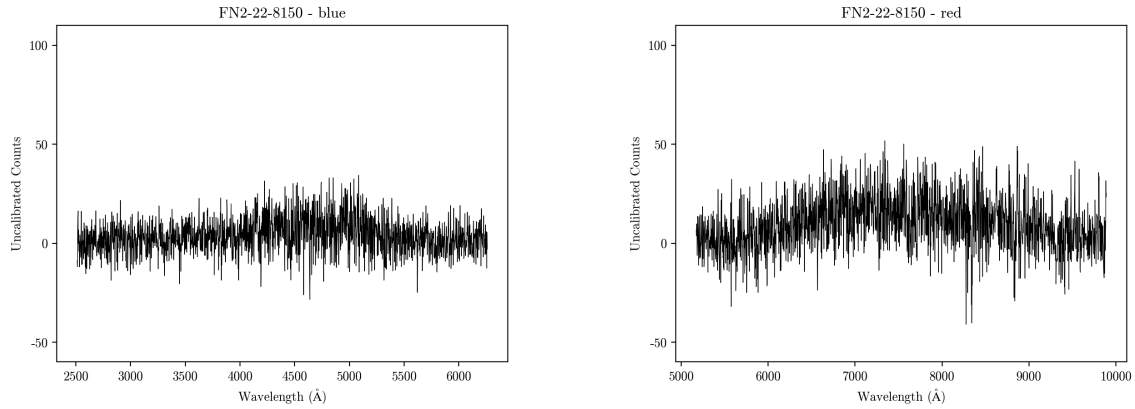

(a) Blue spectrum of FN2-22-8150. **(b)** Red spectrum of FN2-22-8150.

Figure 2.6 Blue and red spectra for FN2-22-8150.

FN8-45-16341

Figure 2.7 shows the blue and red spectra of FN8-45-16341. FN8-45-16341 appears to be a star. FN8-45-16341 falls within the Hα and 2σ regions on the color-color plot. As more of these are observed, it will help us understand the traits found in objects in that region.

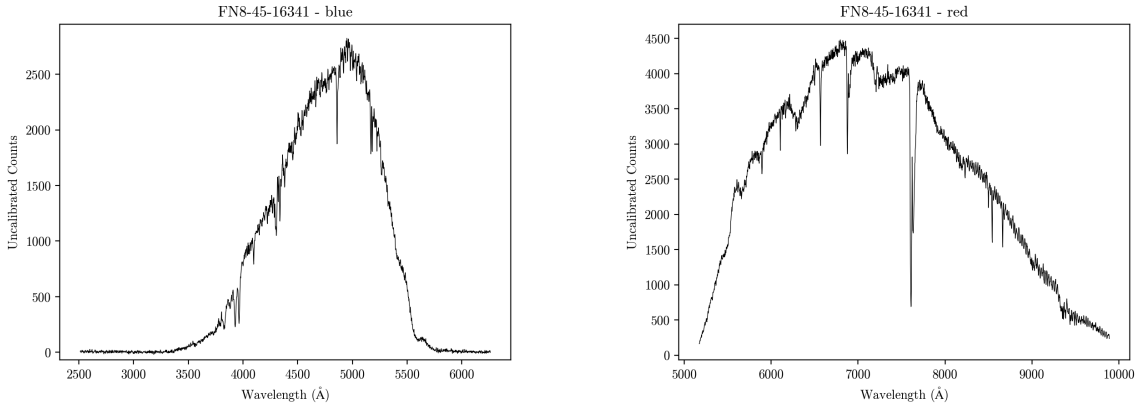

(a) Blue spectrum of FN8-45-16341. **(b)** Red spectrum of FN8-45-16341.

Figure 2.7 Blue and red spectra for FN8-45-16341.

FN8-45-11878

Figure 2.8 shows the blue and red spectra of FN8-45-11878. Based on these spectra extracted for FN8-45-11878, this object is clearly a star.

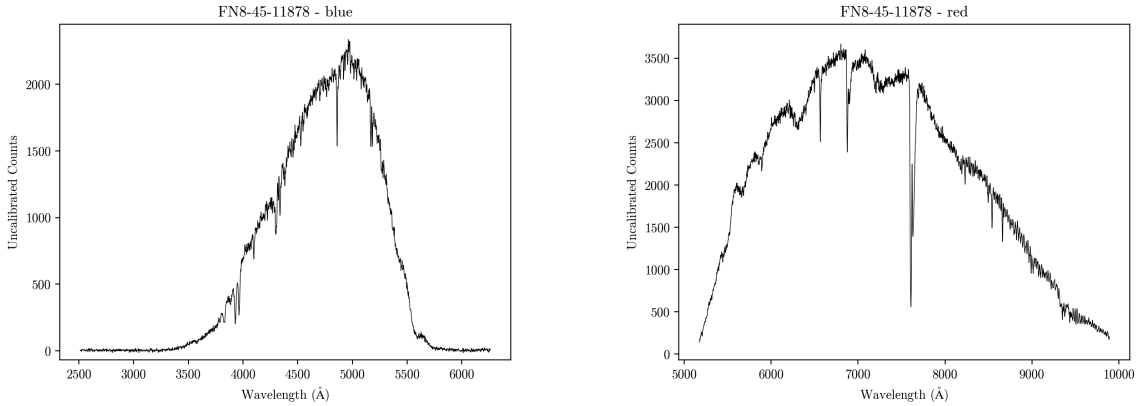

(a) Blue spectrum of FN8-45-11878. **(b)** Red spectrum of FN8-45-11878.

Figure 2.8 Blue and red spectra for FN8-45-11878.

FN8-45-2887

Figures 2.9a and 2.9b show the blue and red spectra of FN8-45-2887, respectively.

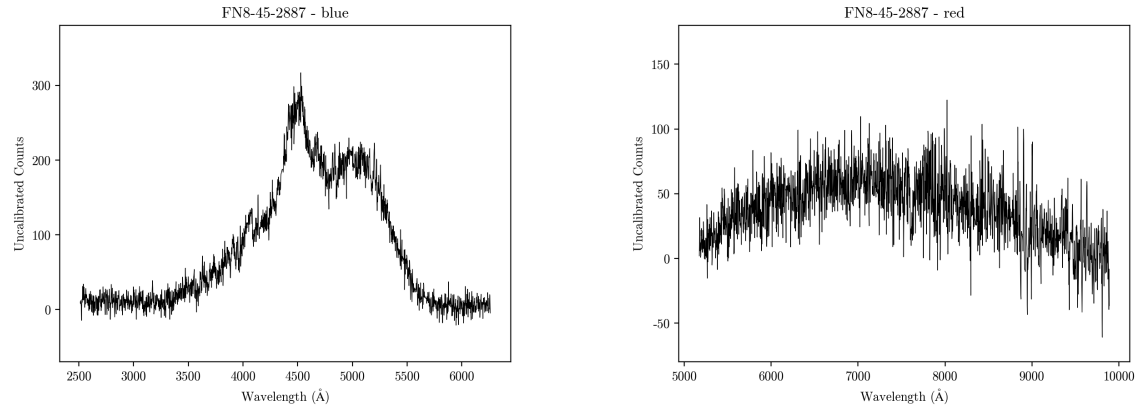

(a) Blue spectrum of FN8-45-2887. **(b)** Red spectrum of FN8-45-2887.

Figure 2.9 Blue and red spectra for FN8-45-2887.

FN2-22-11932

In the red image of FN2-22-11932, no object was visible. An object was visible in the blue, but there were no identified emission lines. Figure 2.10 shows the blue spectrum of FN2-22-11932.

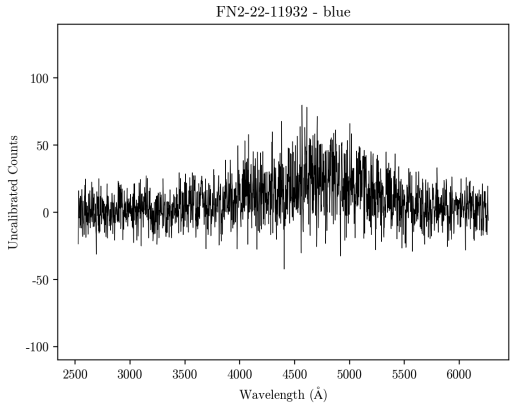

Figure 2.10 Blue spectrum for FN2-22-11932.

FN2-22-6936

Figures 2.11a and 2.11b show the blue and red spectra of FN2-22-6936, respectively.

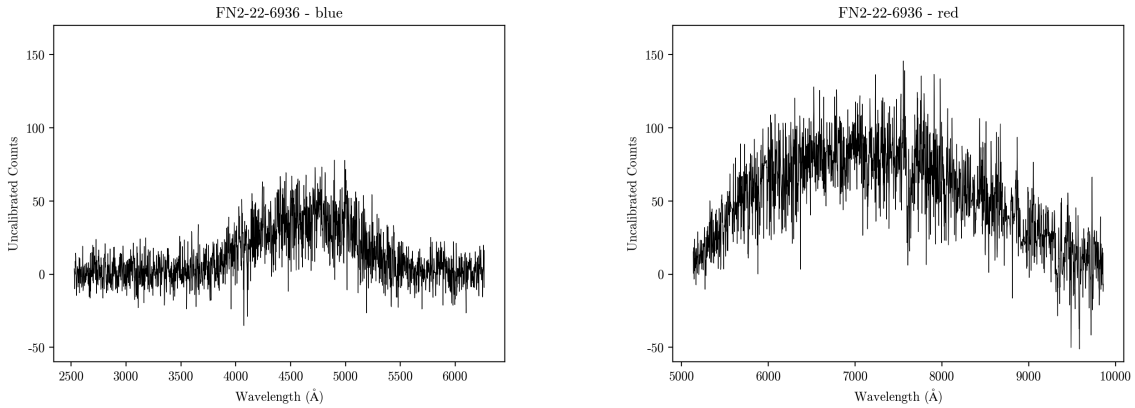

(a) Blue spectrum of FN2-22-6936.

(b) Red spectrum of FN2-22-6936.

Figure 2.11 Blue and red spectra for FN2-22-6936.

FN2-23-4526

Figures 2.12a and 2.12b show the blue and red spectra of FN2-23-4526, respectively.

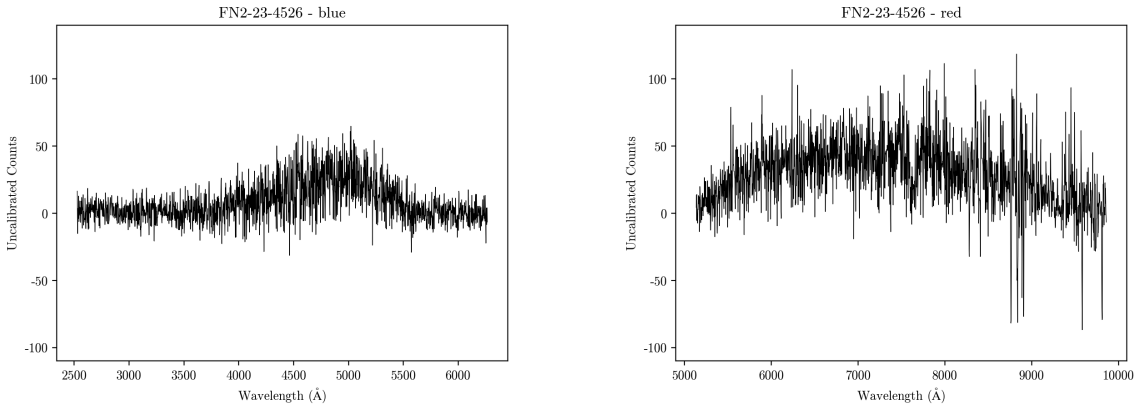

(a) Blue spectrum of FN2-23-4526. **(b)** Red spectrum of FN2-23-4526.

Figure 2.12 Blue and red spectra for FN2-23-4526.

FN2-32-5251

Figures 2.13a and 2.13b show the blue and red spectra of FN2-32-5251, respectively.

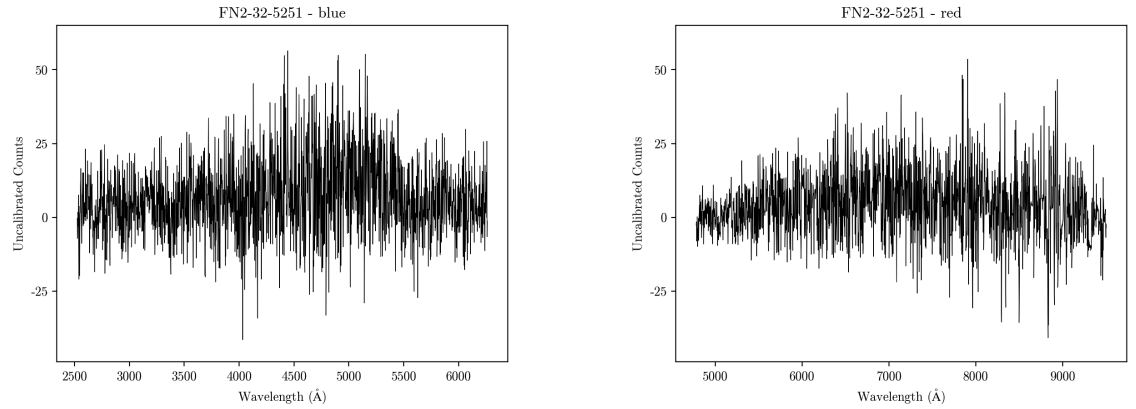

(a) Blue spectrum of FN2-32-5251. **(b)** Red spectrum of FN2-32-5251.

Figure 2.13 Blue and red spectra for FN2-32-5251.

2.2.3 Objects with Emission Outside Bandpass

These objects have prominent emission, but outside the bandpass of the Gaussian filters. Because there is no emission within the Gaussian filters, the object should not have been identified using this method and the presence of emission lines elsewhere in the spectrum appears to be a coincidence.

Hα emission

FN2-23-8674

The location of the Hα line gives the object FN2-23-8674 a redshift of z = 0.107 $\pm$ 0.002. The wavelength and equivalent width of the identified emission lines are in Table 2.4. Figures 2.14a and 2.14b show the blue and red spectra of FN2-23-8674, respectively.

Table 2.4 Emission lines from FN2-23-8674.

Emission	Observed Wavelength (Å)	Equivalent Width (Å)	Notes
[OIII]λ5007	5535.056	12.9376	Very faint
Hα	7265.075	21.6891	

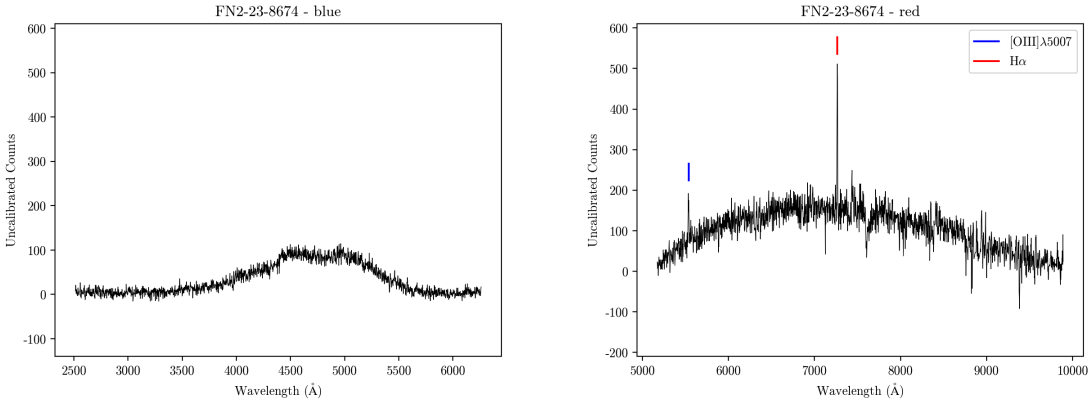

(a) Blue spectrum of FN2-23-8674. **(b)** Red spectrum of FN2-23-8674.

Figure 2.14 Blue and red spectra for FN2-23-8674.

FN2-22-9134

FN2-22-9134 has a redshift of z = 0.2436 $\pm$ 0.0003/0.001 (mean/max). The observed emission lines from both spectra are shown in Table 2.5. The blue and red spectra are shown in Figures 2.15a and 2.15b, respectively.

Table 2.5 Emission lines from FN2-22-9134.

Emission	Observed Wavelength (Å)	Equivalent Width (Å)	Notes
[OII]	4638.793	22.7537	
Hβ	6046.81	8.2962	Faint
[OIII]λ5007	6228.601	7.329	Faint, on a skyline
Hα	8163.903	45.4283	
[NII]λ6584	8190.118	17.0294	

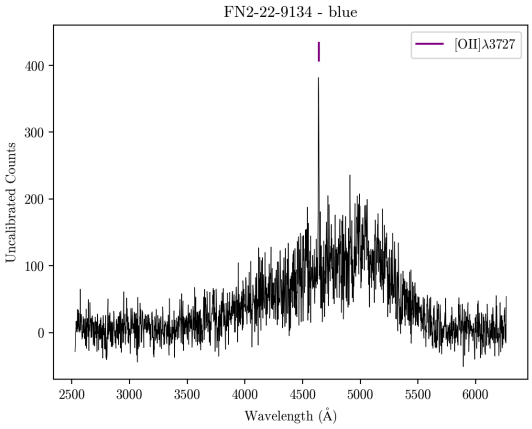

(a) Blue spectrum of FN2-22-9134.

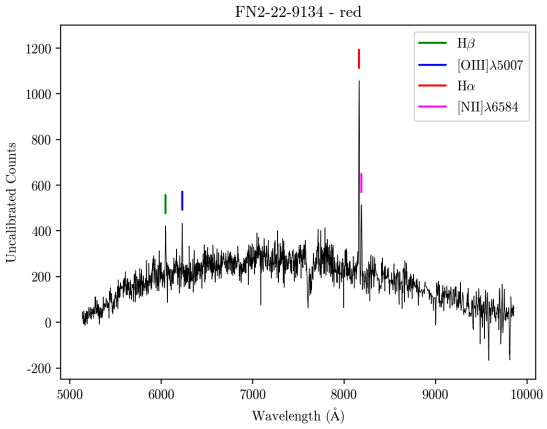

(b) Red spectrum of FN2-22-9134.

Figure 2.15 Blue and red spectra for FN2-22-9134.

Unknown Emission

FN2-23-7651

Only one emission line was found for FN2-23-7651, so the identity of the line could not be deduced. The emission found was on top of a known skyline, so the equivalent width was also questionable. The lone emission line is recorded in Table 2.6. The spectra for this object are shown in Figure 2.16.

Table 2.6 Emission line from FN2-23-7651.

Emission	Observed Wavelength (Å)	Equivalent Width (Å)	Notes
Unknown	7488.505	18.1962	On top of a skyline

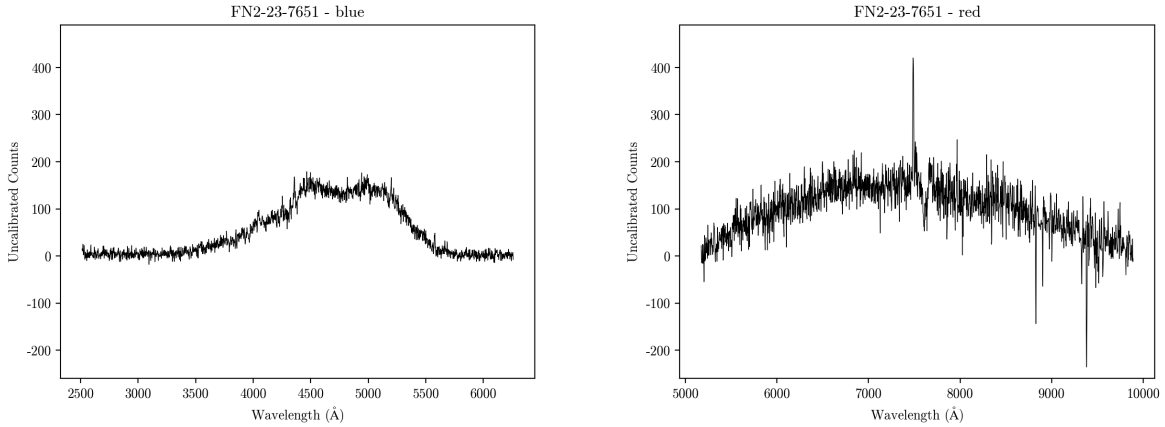

(a) Blue spectrum of FN2-23-7651. **(b)** Red spectrum of FN2-23-7651.

Figure 2.16 Blue and red spectra for FN2-23-7651.

FN2-22-7633

For FN2-22-7633, there was only one emission line identified. Because there were no other emission lines found, the identity of the emission line could not be determined. This emission line is displayed in Table 2.7. The spectra for this object are shown in Figure 2.17.

Table 2.7 Emission line from FN2-22-7633.

Emission	Observed Wavelength (Å)	Equivalent Width (Å)	Notes
Unknown	7502.605	21.8966	

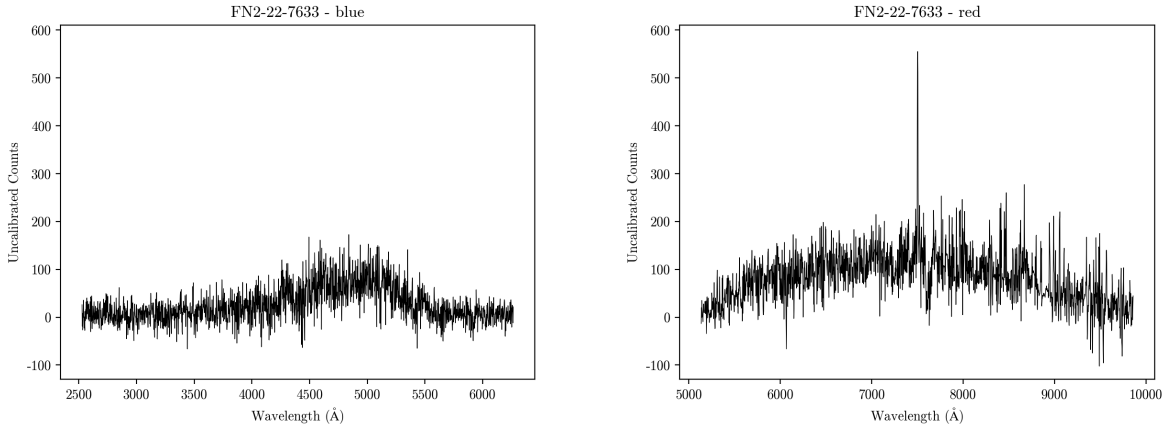

(a) Blue spectrum of FN2-22-7633. **(b)** Red spectrum of FN2-22-7633.

Figure 2.17 Blue and red spectra for FN2-22-7633.

2.2.4 Objects with Emission Inside Bandpass

These objects have emission present within the bandpass of the Gaussian filters. This supports the accuracy of the method.

Hα emission

FN8-45-6206

Based on the finder chart, Figure A.4e, this object appears to be an edge on spiral galaxy with a knot in one of the arms. I reduced and processed the spectra for both the nucleus of the object and the

knot. For distinction, these are referred to as FN8-45-6206-n for the nucleus and FN8-45-6206-k for the knot.

Both of these spectra had an Hα emission line within the bandpass of the Gaussian filters. The identified emission lines are for the nucleus and the knot are in Tables 2.8 and 2.9, respectively.

The redshift calculated for FN8-45-6206-n is cz = 6,969 $\pm$ 95/182km·s^{-1} (mean/max), while the redshift of FN8-45-6206-k was calculated at cz = 7,085 $\pm$ 63/120km·s^{-1} (mean/max). Both of these calculated redshifts place the galaxy behind the void FN8. If these two signals originated from the same object, as expected, then the two redshift values should be the same. There is some variance between the two, but they are within the maximum error for both, indicating that it is still reasonable for them to be from the same object. It is also possible that variance between the calculated redshift values is due to the rotation of the knot around the nucleus of the spiral galaxy.

The spectra for FN8-45-6206-n are given in Figure 2.18, while the spectra for FN8-45-6206-k are in Figure 2.19. Because the Hα emission line in Figure 2.19b dwarfs the rest of the spectrum, Figure 2.20 shows the same red spectrum zoomed in to get a better view of the other spectral features.

Table 2.8 Emission lines from FN8-45-6206-n.

Emission	Observed Wavelength (Å)	Equivalent Width (Å)	Notes
Hβ	4974.144	6.8501	
[OIII]λ5007	5121.614	2.6885	
Hα	6717.202	48.1103	
[NII]λ6584	6738.229	14.5316	

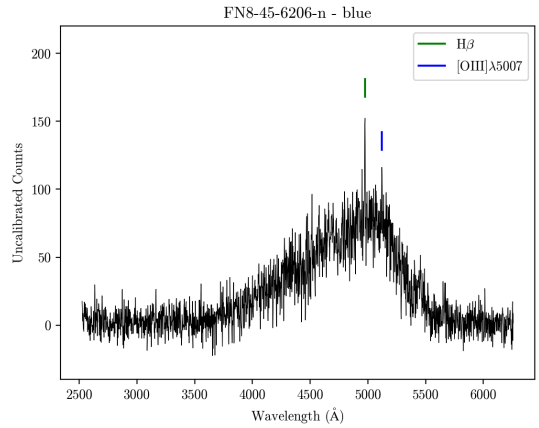

(a) Blue spectrum of FN8-45-6206-n.

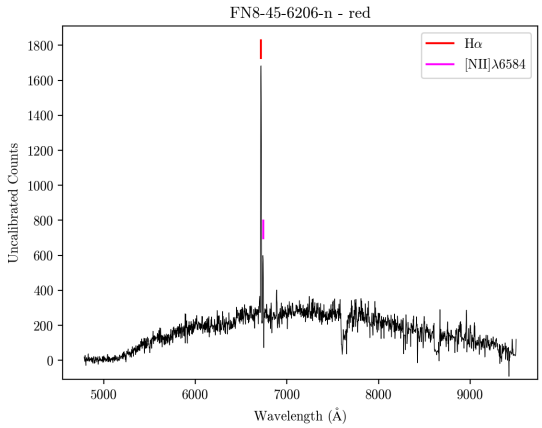

(b) Red spectrum of FN8-45-6206-n.

Figure 2.18 Blue and red spectra for FN8-45-6206-n.

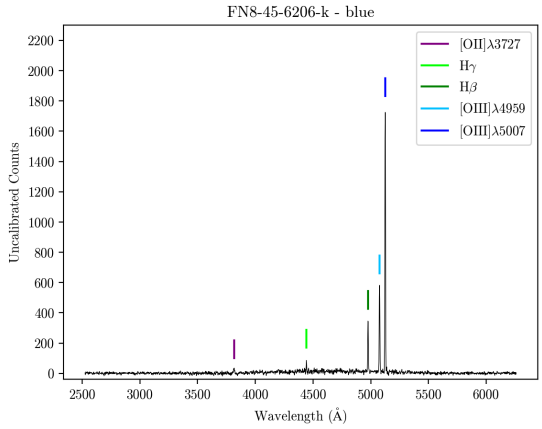

(a) Blue spectrum of FN8-45-6206-k.

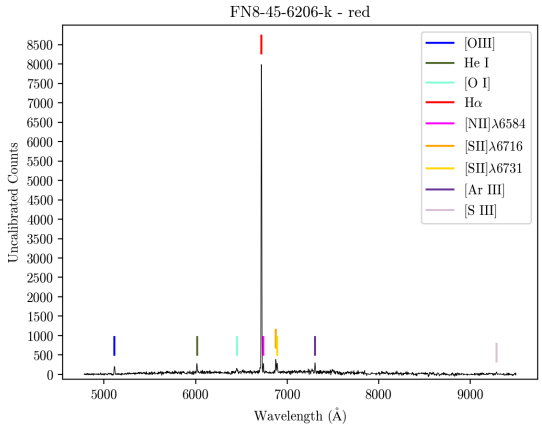

(b) Red spectrum of FN8-45-6206-k.

Figure 2.19 Blue and red spectra for FN8-45-6206-k.

Table 2.9 Emission lines from FN8-45-6206-k.

Emission	Observed Wavelength (Å)	Equivalent Width (Å)	Notes
[OII]λ3727	3815.937	54.0764	
Hγ	4442.559	18.07	
Hβ	4976.416	205.0606	
[OIII]λ4959	5076.111	311.24	
[OIII]λ5007	5125.209	1095.386	
HeI	6016.173	51.8886	
[OI]	6452.105	34.8388	
Hα	6719.759	1211.18	
[NII]λ6584	6740.247	18.7253	
[SII]λ6716	6877.293	56.716	
[SII]λ6731	6891.772	48.1438	
[ArIII]	7305.483	28.3101	
[SIII]	9286.196	217.5596	

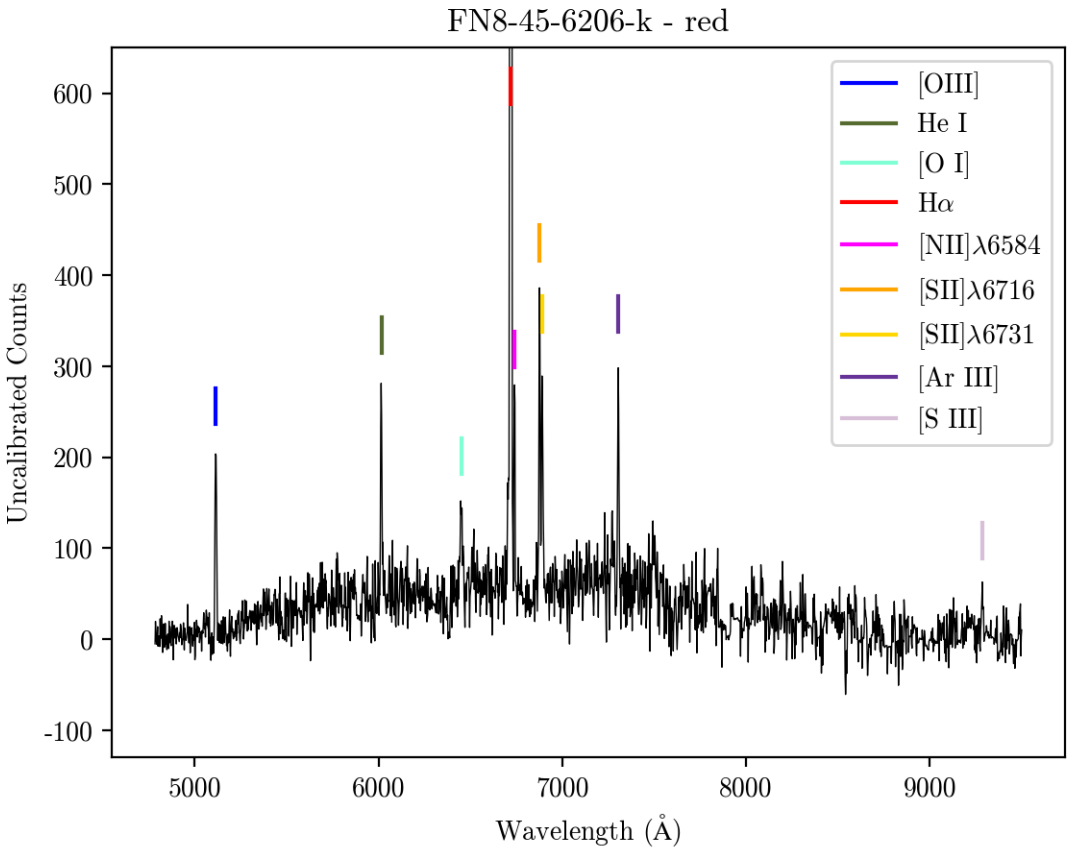

Figure 2.20 Close-up of the red spectrum of FN8-45-6206-k.

FN8-45-7617

FN8-45-7617 has Hα emission visible just within the bandpass of the Gaussian filters. This puts the object at a distance of cz = 6,997 $\pm$ 62km·s^{-1} which is just past the void FN8, which extends as far as cz = 6810km·s^{-1}. This finding implies that the Gaussian filter method was able to accurately identify an object with Hα emission within the redshift region being searched, but the distance indicates that is not within the center of the void itself. The emission lines visible are shown in Table 2.10. The blue and red spectra are shown in Figures 2.21a and 2.21b, respectively.

Table 2.10 Emission lines from FN8-45-7617.

Emission	Observed Wavelength (Å)	Equivalent Width (Å)	Notes
[OIII]λ5007	5126.164	13.9005	
Hα	6717.83	31.2131	

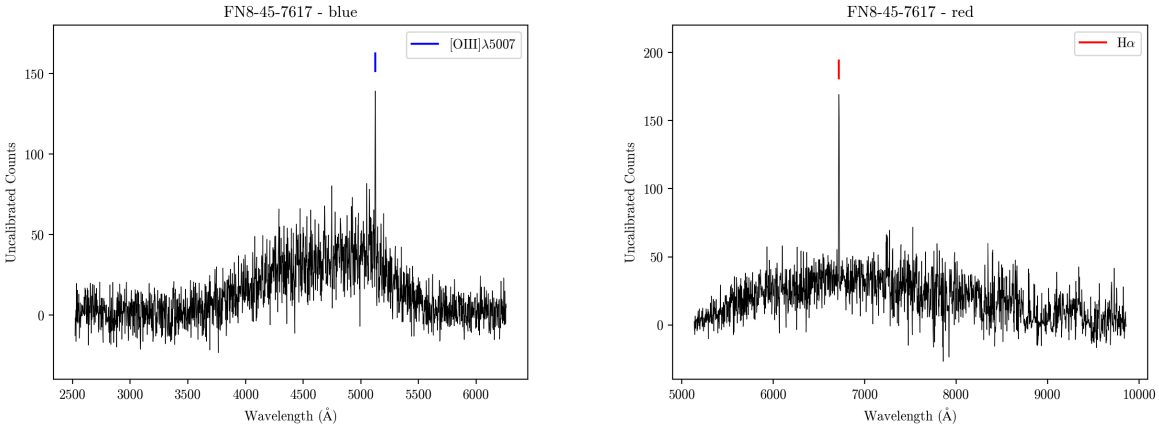

(a) Blue spectrum of FN8-45-7617.

(b) Red spectrum of FN8-45-7617.

Figure 2.21 Blue and red spectra for FN8-45-7617.

FN2-23-7179

Based on the location of the Hα emission line, FN2-23-7179 appears to be very close to us, with a redshift of only cz = 35.8 $\pm$ 53/103km·s^{-1} (mean/max). The emission lines present are shown in Table 2.11. The spectra are in Figure 2.22.

Table 2.11 Emission lines from FN2-23-7179.

Emission	Observed Wavelength (Å)	Equivalent Width (Å)	Notes
Hβ	4864.128	30.6667	
He I λ5875	5875.319	26.0923	
Hα	6565.393	95.4642	
He I λ6678	6681.238	16.6724	
He I λ7065	7065.937	18.8033	

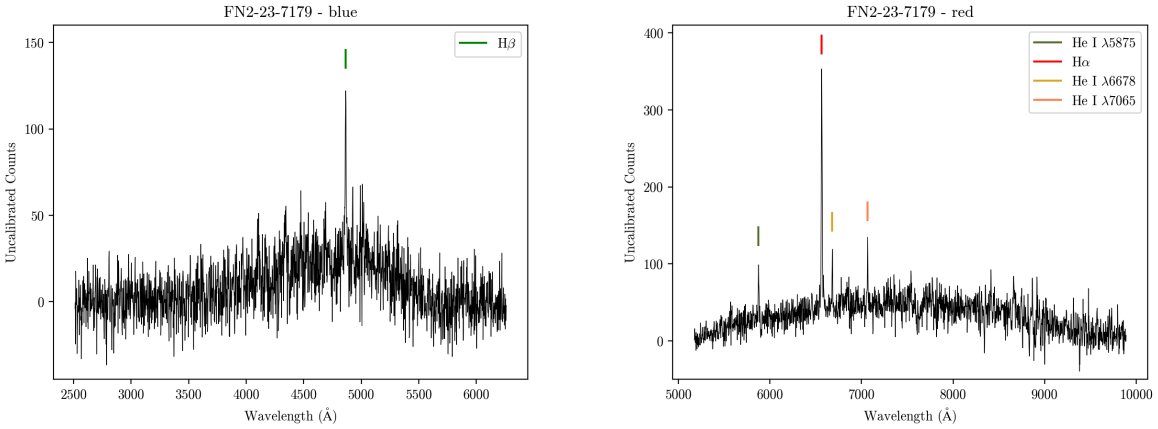

(a) Blue spectrum of FN2-23-7179.

(b) Red spectrum of FN2-23-7179.

Figure 2.22 Blue and red spectra for FN2-23-7179.

Using Equation 1.3, the redshift estimated above gives a distance of about 51kpc, which is comparable to the distance to the Large Magellanic Cloud (LMC), 49.97kpc. This indicates that, based purely on distance, object FN2-23-7179 is likely a dwarf galaxy in the Local Group.

Local Group dwarf galaxies often have an abundance of oxygen, and sometimes nitrogen, sulphur or helium (Mateo 1998). FN2-23-7179 did not have any visible oxygen lines, but as can be seen in Table 2.11, there are two helium emission lines present. The presence of helium in FN2-23-7179 may imply a similarity between Local Group dwarf galaxies and FN2-23-7179.

The V-band apparent magnitudes of Local Group dwarf galaxies are between 4.0 and 15.15 and the V-band absolute magnitudes are between -18.0 and -8.8 (Mateo 1998), while FN2-23-7179 has an r'-band apparent magnitude of 18.5 and an r'-band absolute magnitude of -0.038. The magnitudes are in different filters, but the differences between FN2-23-7179 and Local Group dwarfs are so large that we can safely infer qualitative conclusions by comparing them. The apparent and absolute magnitudes of FN2-23-7179 are many magnitudes dimmer than the Local Group dwarf galaxies, showing that this object is much fainter than the Local Group dwarfs. It is, however, definitely within the radius of the Local Group, because the dwarf galaxies within the Local Group span 8kpc to 1590kpc from the Milky Way, and FN2-23-7179 is only 51 kpc from us.

[OIII] emission

FN8-34-10395

FN8-34-10395 has an [OIII] emission line in the Gaussian filters, giving the object a redshift of z = 0.340 $\pm$ 0.0002/0.0004 (mean/max). The observed wavelengths and equivalent widths of the identified emission lines in the blue and red spectra are given in Table 2.12. For the emission line on a skyline, which is indicated in Table 2.12, the equivalent width calculated has very high error, as it was affected by the presence of the skyline. The spectra are shown in Figure 2.23.

Table 2.12 Emission lines from FN8-34-10395.

Emission	Observed Wavelength (Å)	Equivalent Width (Å)	Notes
[OII]	4995.381	23.4202	
Hβ	6517.633	20.1668	
[OIII]λ4959	6649.586	10.5737	
[OIII]λ5007	6712.823	44.002	
Hα	8796.087	129.0285	
[SII]λ6716	9003.867	85.3501	On a skyline
[SII]λ6731	9023.724	44.7795	Very faint

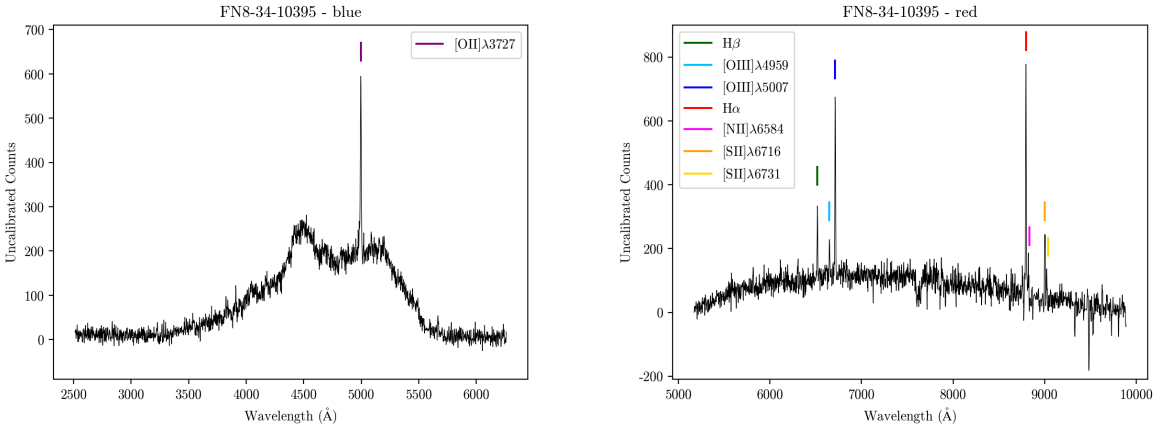

(a) Blue spectrum of FN8-34-10395.

(b) Red spectrum of FN8-34-10395.

Figure 2.23 Blue and red spectra for FN8-34-10395.

FN8-53-16430

FN8-53-16430 has [OIII] emission within the bandpass of the Gaussian filters, indicating the method was able to correctly identify emission. This object has a redshift of z = 0.333 $\pm$ 0.0004/0.0011 (mean/max). The observed emission lines are in Table 2.13 and the spectra are in Figure 2.24.

Table 2.13 Emission lines from FN8-53-16430.

Emission	Observed Wavelength (Å)	Equivalent Width (Å)	Notes
[OII]	4970.921	55.9344	
Hβ	6479.12	20.5444	
[OIII]λ4959	6610.387	15.323	
[OIII]λ5007	6673.897	50.1097	
Hα	8748.846	263.4125	

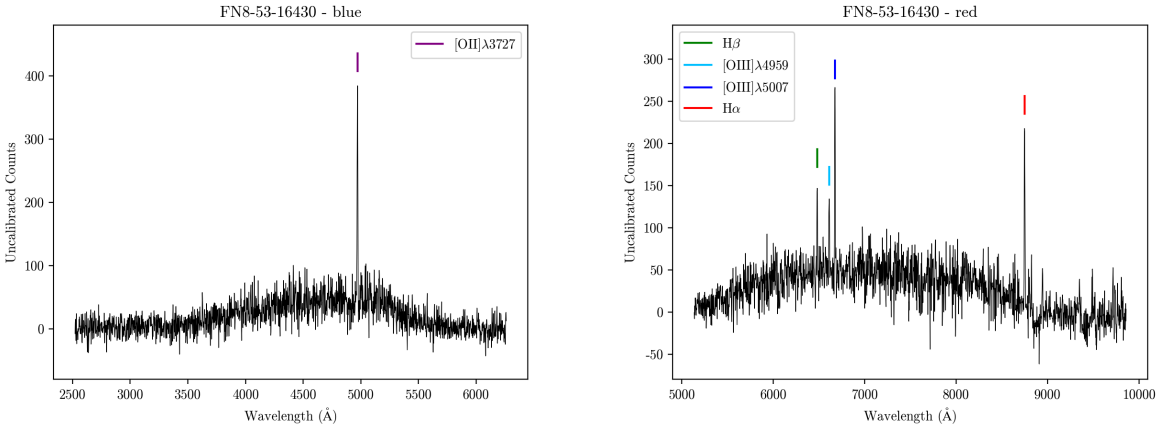

(a) Blue spectrum of FN8-53-16430. **(b)** Red spectrum of FN8-53-16430.

Figure 2.24 Blue and red spectra for FN8-53-16430.

FN8-34-11439

The emission from the [OIII] doublet puts FN8-34-11439 at a distance of z = 0.331 $\pm$ 0.0004/0.0013 (mean/max). Table 2.14 gives the emission lines found in the spectrum of FN8-34-11439. Figure 2.25 gives the observed spectra for FN8-34-11439.

Table 2.14 Emission lines from FN8-34-11439.

Emission	Observed Wavelength (Å)	Equivalent Width (Å)	Notes
[OII]	4964.203	75.4053	
Hβ	6470.015	47.7159	
[OIII]λ4959	6599.605	30.8537	
[OIII]λ5007	6663.935	90.3336	
Hα	8736.218	107.1414	

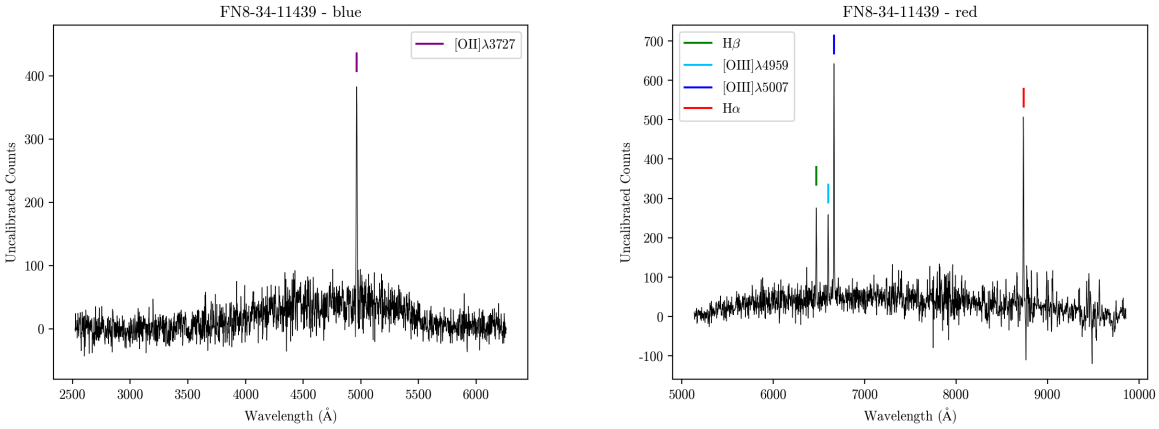

(a) Blue spectrum of FN8-34-11439.

(b) Red spectrum of FN8-34-11439.

Figure 2.25 Blue and red spectra for FN8-34-11439.

FN8-43-12351

FN8-43-12351 falls at a distance of z = 0.331 $\pm$ 0.0003/0.0008 (mean/max), as measured by the [OIII] doublet. The emission lines observed are given in Table 2.15. The blue and red spectra of FN8-43-12351 are given in Figures 2.26a and 2.26b, respectively.

Table 2.15 Emission lines from FN8-43-12351.

Emission	Observed Wavelength (Å)	Equivalent Width (Å)	Notes
[OII]	4965.157	88.5061	
Hβ	6473.759	31.4301	
[OIII]λ4959	6604.081	23.3071	
[OIII]λ5007	6667.7	70.2507	
Hα	8741.444	85.845	

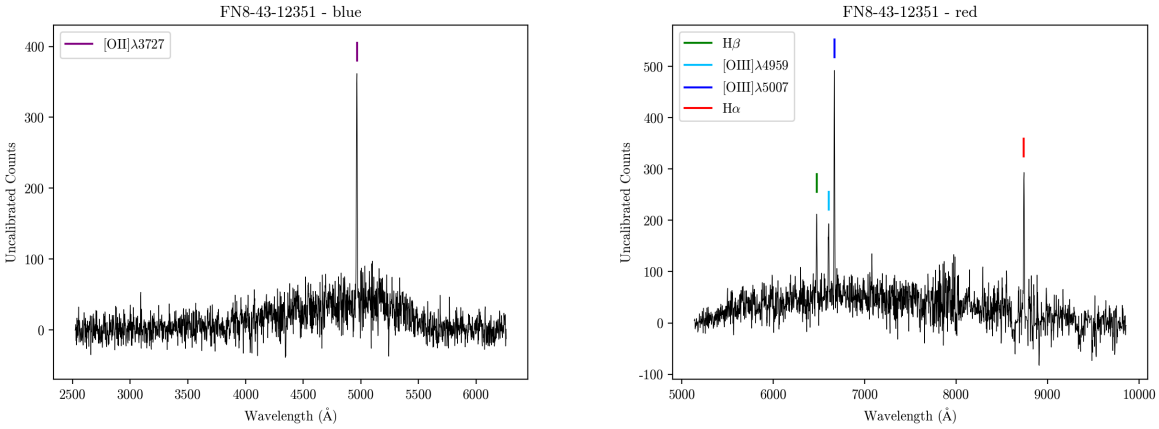

(a) Blue spectrum of FN8-43-12351.

(b) Red spectrum of FN8-43-12351.

Figure 2.26 Blue and red spectra for FN8-43-12351.

FN8-34-8185

FN8-34-8185 has emission from the [OIII] doublet within the bandpass of the Gaussian filters, indicating the object has a distance of z = 0.327 $\pm$ 0.0003/0.0007 (mean/max). The emission lines from the blue and red spectra are shown in Table 2.16 and Figure 2.27 shows the spectra of FN8-34-8185.

Table 2.16 Emission lines from FN8-34-8185.

Emission	Observed Wavelength (Å)	Equivalent Width (Å)	Notes
[OII]	4949.886	72.3646	
Hβ	6454.934	21.8539	
[OIII]λ4959	6647.63	64.8449	
[OIII]λ5007	6667.7	70.2507	
Hα	8716.039	78.3111	

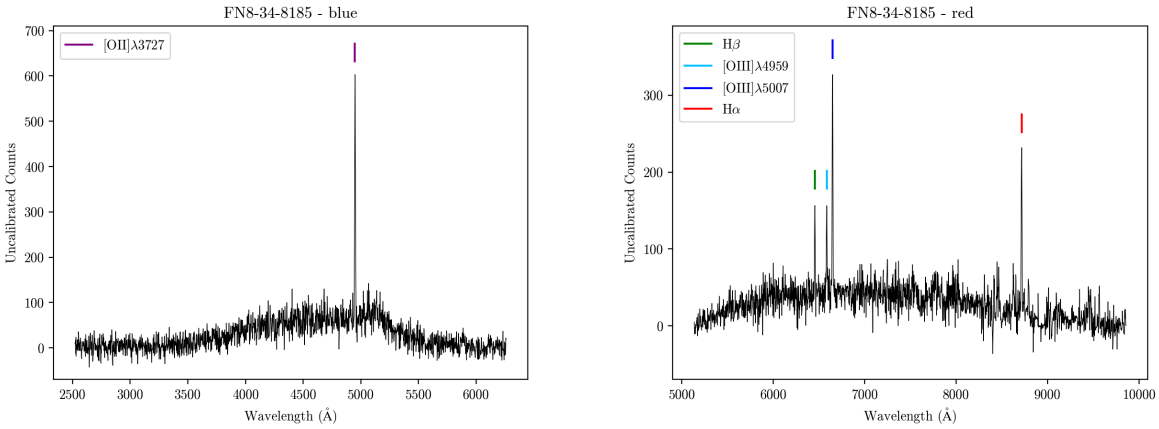

(a) Blue spectrum of FN8-34-8185. **(b)** Red spectrum of FN8-34-8185.

Figure 2.27 Blue and red spectra for FN8-34-8185.

FN8-34-15362

Many of the spectral lines in FN8-34-15362 appeared spread or split in a way that could indicate rotation. The spectra can be seen in Figure 2.28. In Figure 2.28a, the [OII] line appears split. This can be better viewed in Figure 2.29.The redshift calculated from the location of the [OIII] doublet is z = 0.341 $\pm$ 0.0003/0.0004 (mean/max). The positions and equivalent widths of the emission lines from both spectra are given in Table 2.17.

Table 2.17 Emission lines from FN8-34-15362.

Emission	Observed Wavelength (Å)	Equivalent Width (Å)	Notes
[OII]	4999.07	32.9778	
Hβ	6521.889	8.6343	
[OIII]λ4959	6650.105	16.3273	
[OIII]λ5007	6716.411	46.0246	
Hα	8805.426	25.3987	

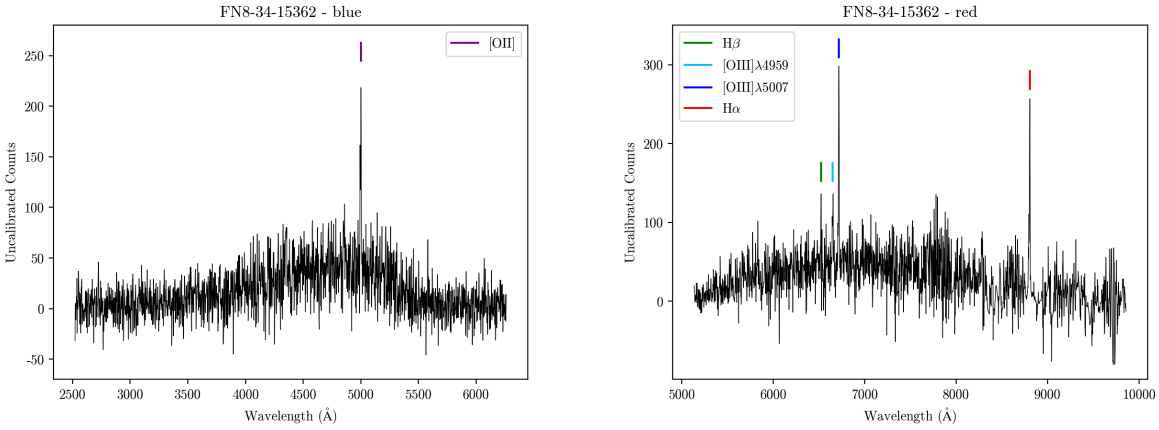

(a) Blue spectrum of FN8-34-15362.

(b) Red spectrum of FN8-34-15362.

Figure 2.28 Blue and red spectra for FN8-34-15362.

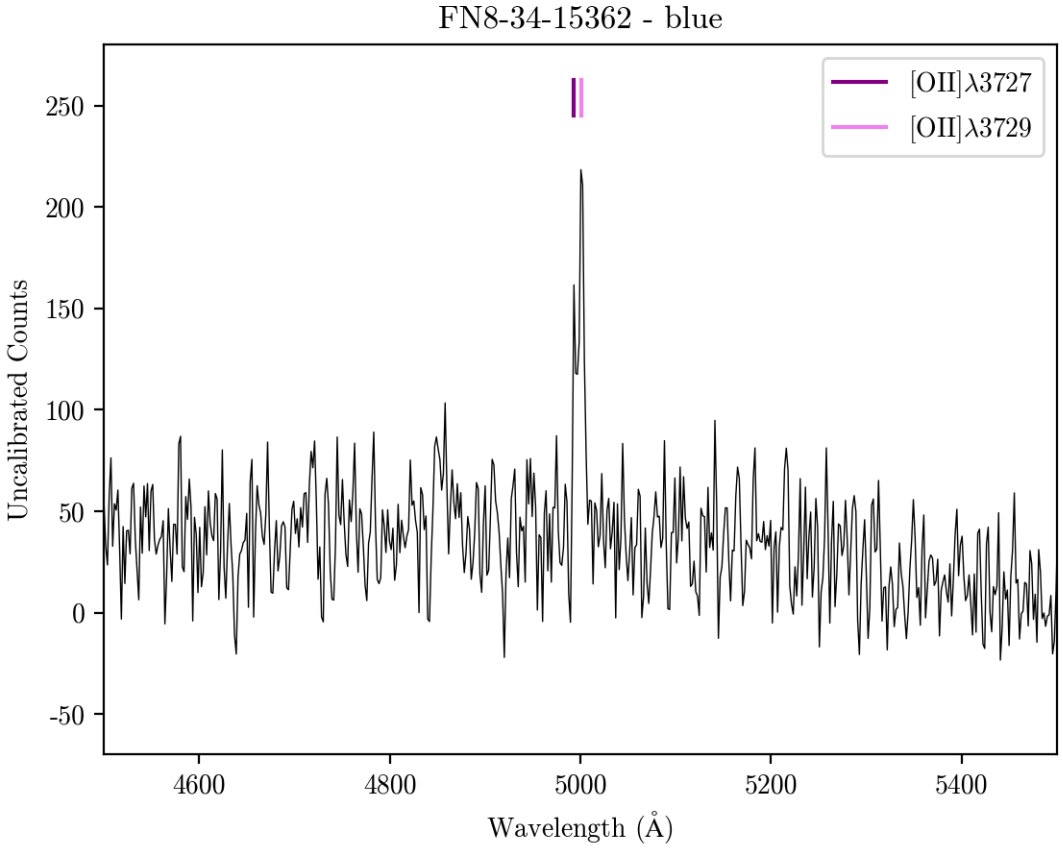

Figure 2.29 Close-up of the [OII] emission for object FN8-34-15362. The [OII] emission appears split, perhaps from rotation and because [OII] is a doublet.

Hβ emission

FN8-34-6530

FN8-34-6530 has emission within the bandpass of the Gaussian filters from the Hβ line, putting the object at a redshift of z = 0.368 $\pm$ 0.0002/0.0006 (mean/max). I had initially neglected to take Hβ emission into account, but this shows that Hβ galaxies can also contaminate the filter bandpass. The observed emission lines are listed in Table 2.18. The spectra are shown in Figure 2.30.

Table 2.18 Emission lines from FN8-34-6530.

Emission	Observed Wavelength (Å)	Equivalent Width (Å)	Notes
[OII]	5098.146	85.0414	
Hβ	6649.844	28.1698	
[OIII]λ4959	6783.382	26.4016	
[OIII]λ5007	6848.683	82.6855	
Hα	8981.034	94.7697	

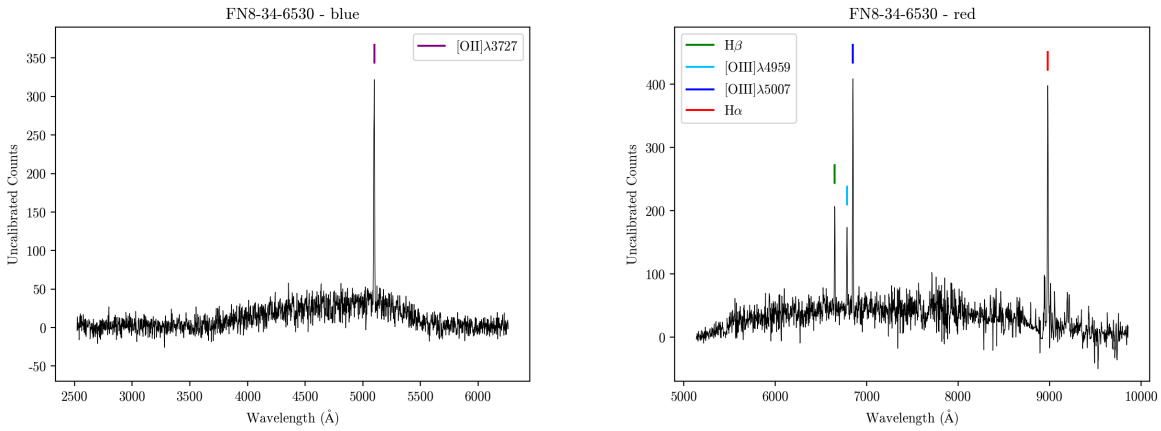

(a) Blue spectrum of FN8-34-6530.

(b) Red spectrum of FN8-34-6530.

Figure 2.30 Blue and red spectra for FN8-34-6530.

Hγ emission

FN8-53-15443

FN8-53-15443 has emission from the Hγ transition within the bandpass of the Gaussian filters, putting it at a distance of z = 0.548 $\pm$ 0.0004/0.0005 (mean/max). This is an important object, as I had not anticipated that Hγ would be identified in the Gaussian filters. The emission features observed are in Table 2.19. Some of the features were on top of skylines, which would greatly increase the error of the equivalent width. These lines are noted in the table. Figures 2.31a and 2.31b are the blue and red spectra, respectively.

Table 2.19 Emission lines from FN8-53-15443.

Emission	Observed Wavelength (Å)	Equivalent Width (Å)	z	Notes
[OII]λ3727	5767.441	115.6597		
Hγ	6720.558	21.9446		
Hβ	7524.983	65.0322		On top of a skyline
[OIII]λ4959	7676.298	70.8444		
[OIII]λ5007	7750.375	114.0274		On top of a skyline

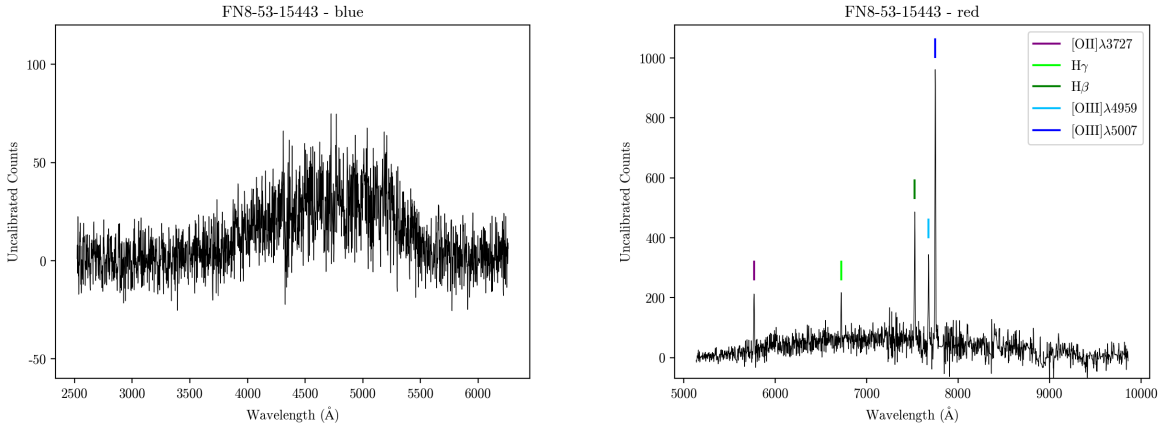

(a) Blue spectrum of FN8-53-15443. **(b)** Red spectrum of FN8-53-15443.

Figure 2.31 Blue and red spectra for FN8-53-15443.

[OII] emission

FN8-53-4906

FN8-53-4906 has [OII] emission within the bandpass of the Gaussian filters, which puts the redshift of the object at z = 0.799 $\pm$ 0.0019/0.0036 (mean/max). The observed emission lines are shown in Table 2.20. One emission line was on top of a skyline, as noted in the table, so the equivalent width calculated is less certain. The spectra are shown in Figure 2.32.

Table 2.20 Emission lines from FN8-53-4906.

Emission	Observed Wavelength (Å)	Equivalent Width (Å)	Notes
[OII]λ3727	6704.079	155.4123	
Hβ	8764.227	839.8542	Redder than expected
[OIII]λ4959	8914.356	106.219	Bluer than expected
[OIII]λ5007	9005.838	254.6408	On top of skyline

The Hβ line in FN8-53-4906 is broadened, which could indicate that the object is an Active Galactic Nucleus (AGN). The location of the spectral line identified as Hβ, however, leads to some uncertainty. Figure 2.33 shows a portion of the red spectrum of FN8-53-4906 focused on the Hβ line and the neighboring [OIII]λ4959 line, identified with short markers, as labeled in the legend. There are also long markers that span the height of the figure indicating where Hβ and [OIII]λ4959 would be, as calculated from the redshift of the [OII] doublet. The location of the emission identified as [OIII]λ4959 is close enough to the calculated value that this classification seems reasonable, but the calculated location of the Hβ line is offset enough from the center of the broad line (about 17Å) to cause some questions. This difference caused the large error in the redshift of FN8-53-4906 and is big enough to indicate that either this line is not Hβ as presumed, or there is another factor affecting the redshift or shape of the emission. This could be rotation within the galaxy or the result of a merger with another galaxy. It could also be from asymmetric obscuration of the emission line, which can occur in AGN. This asymmetry is thought to originate from one side of the accretion disk being blocked more than the other. So, perhaps for this object, the light from the blue-shifted side has more extinction than that from the red-shifted side.

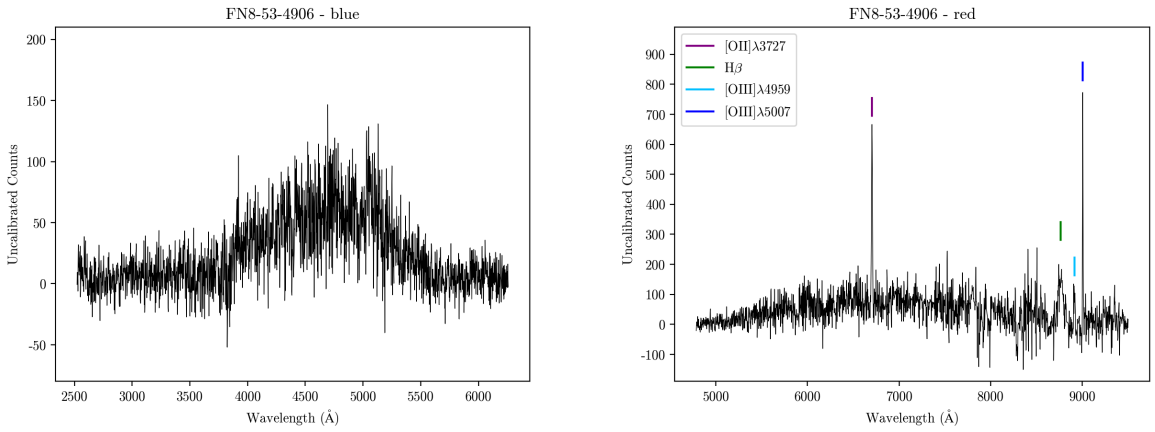

(a) Blue spectrum of FN8-53-4906. **(b)** Red spectrum of FN8-53-4906.

Figure 2.32 Blue and red spectra for FN8-53-4906.

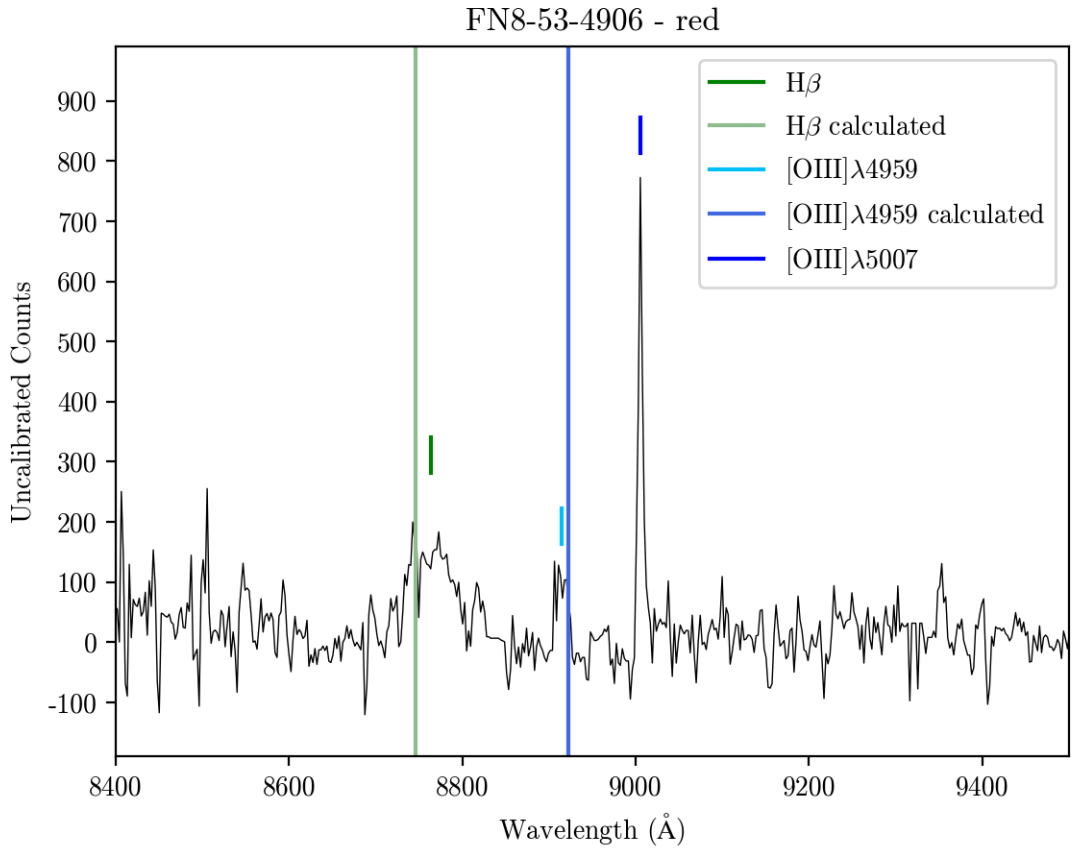

Figure 2.33 Close-up of the red spectrum of FN8-53-4906 focused on the Hβ and [OIII]λ4959 lines. The markers that span the height of the figure are the calculated locations of Hβ and [OIII]λ4959 based on the redshift of [OII].

Unknown Emission

FN8-34-4185

FN8-34-4185 has emission within the bandpass of the Gaussian filters, indicating that the Gaussian filter method correctly identified that there was an emission line. The identity of the line could not be determined because there was only one spectral feature identified. The emission line is shown in Table 2.21. The blue and red spectra are shown in Figures 2.34a and 2.34b, respectively.

Table 2.21 Emission line from FN8-34-4185.

Emission	Observed Wavelength (Å)	Equivalent Width (Å)	Notes
Unknown	6717.211	36.3402	

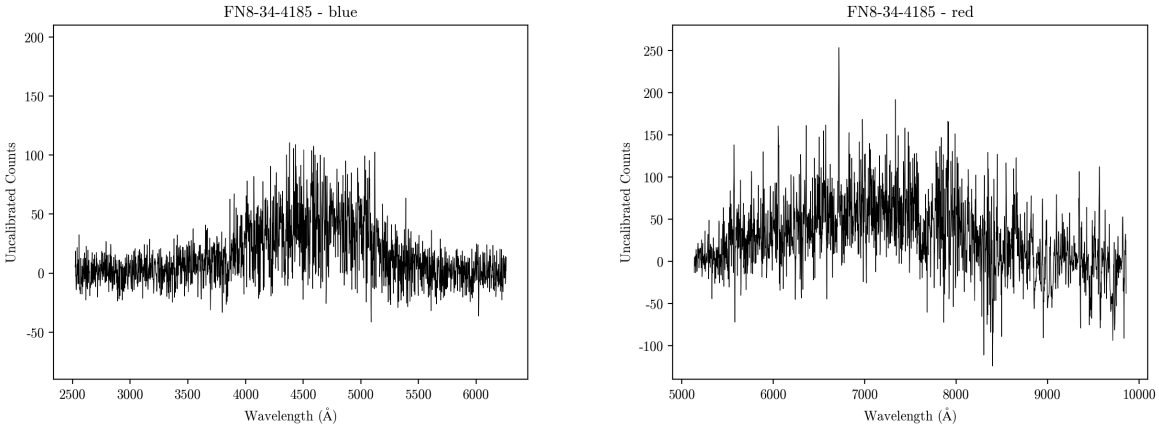

(a) Blue spectrum of FN8-34-4185. **(b)** Red spectrum of FN8-34-4185.

Figure 2.34 Blue and red spectra for FN8-34-4185.

Chapter 3

Ramp Filters Technique

3.1 Survey Methods

To continue to improve the ramp filter method of determining redshift, a survey of objects with a known redshift is required. Fifty-three objects were observed using the ramp filter set described in Section 1.6.2 at West Mountain Observatory (WMO) on a 0.91-meter f/5.5 Ritchey Chretien telescope using an FLI PL3041-UV CCD with a 2048 x 2048 imaging array with 15-micron pixels. The filters used were the same red- and blue-sloping filters described in Section 1.6.2, but a new continuum filter was chosen based on the work of Lesser et al. (2019) and Steele (2021). The continuum filter used was a combination of two filters: a TECHSPEC Orange cutoff imaging filter and a 1mm GG400 Shott glass filter. The TECHSPEC filter provided the bandpass required while the Shott filter made it parfocal with the ramp filters. The transmission of the ramp filters and the new continuum filter are shown in Figure 3.1.

Objects were chosen from the Sloan Digital Sky Survey (SDSS) Data Release 16 (Blanton et al. 2017) and had to fit specific criteria. Each galaxy needed to be at a redshift of $0.01 < z < 0.03$, have an Hα emission line with an equivalent width stronger than 10Å and have an r-band magnitude

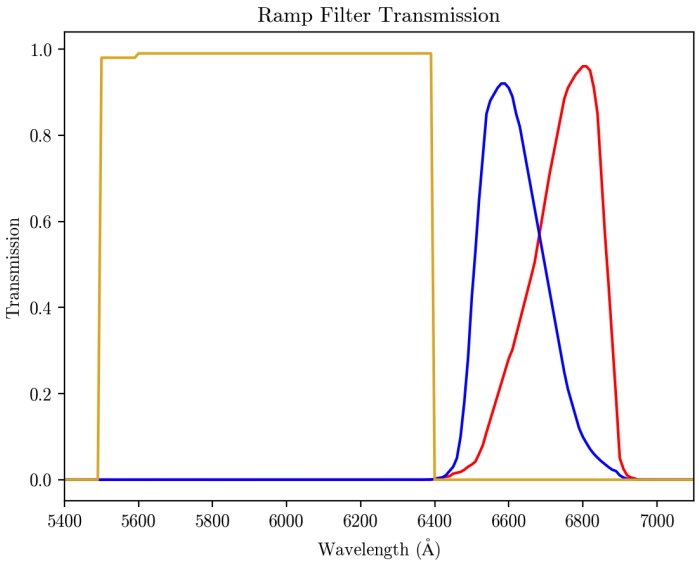

Figure 3.1 Transmission of the filters used in observations. The yellow curve is the continuum filter, the blue curve is the blue-sloping (BS) filter and the red curve is the red-sloping (RS) filter.

brighter than 16. There were far too many SDSS objects that fit this criteria than could be reasonably observed in the time available (more than 5,000 objects), but all were downloaded from SDSS to narrow down further.

These objects were divided into three bins, based on the strength of the emission line. Galaxies with an equivalent width between 10Å and 20Å were put into Bin 1, those with an equivalent width between 20Å and 40Å were put into Bin 2 and those with an equivalent width higher than 40Å were put into Bin 3. These bins were used to ensure objects with a range of line strengths were observed so the method could be tested in these varying circumstances.

The final target list was chosen based on visibility for the time and location of observations and ensuring a spread of redshift between 0.01 and 0.03, with priority given to brighter objects, for ease of observation. All objects in the target list had an r magnitude brighter than 14. The galaxies observed are listed in Table 3.1, with the dates of observation listed.

Table 3.1 Objects observed at WMO. Column 1 gives the identifier for the object (within this project only). Columns 2 and 3 give the right ascension and declination. Column 4 is the magnitude in the r band from SDSS. Column 5 is the redshift (z) from SDSS. Column 6 is the equivalent width of the Hα emission line in angstroms from SDSS. Column 7 indicates the bin the object was sorted into, column 8 is the size of the aperture in arcseconds and column 9 gives the UTC date this object was observed at WMO.

ID	RA	Dec	r (mag)	redshift (z)	Hα EW (Å)	Bin	Aperture (")	Obs date
B1-1	$14^h41^m32^s.03$	$44°30'46''.0$	12.9	0.0109	15.7	1	6.1	07/07/20
B1-2	$14^h32^m39^s.84$	$36°18'08''.0$	12.5	0.0132	12.6	1	9.15	07/08/20
B1-3	$15^h42^m15^s.48$	$39°59'01''.4$	13.8	0.0150	14.2	1	6.1	06/23/20
B1-4	$15^h15^m05^s.56$	$43°09'01''.9$	13.9	0.0179	13.0	1	7.32	06/23/20
B1-5	$15^h30^m36^s.59$	$42°43'01''.7$	13.4	0.0198	13.1	1	12.2	07/07/20
B1-6	$13^h19^m03^s.11$	$39°35'21''.6$	13.9	0.0237	11.0	1	7.32	07/07/20
B1-7	$14^h00^m45^s.80$	$30°04'33''.5$	13.7	0.0273	19.4	1	9.15	06/23/20
B1-8	$14^h35^m18^s.38$	$35°07'07''.5$	13.7	0.0284	16.8	1	9.15	06/23/20
B1-09	$23^h32^m24^s.44$	$15°50'52''.7$	13.0	0.0135	10.0	1	6.1	09/13/20
B1-10	$00^h43^m32^s.39$	$14°20'33''.2$	12.5	0.0148	18.1	1	12.2	09/12/20
B1-11	$23^h14^m13^s.19$	$13°25'35''.0$	13.2	0.0157	17.4	1	4.88	09/20/20
B1-12	$01^h12^m48^s.61$	$-01°42'35''.4$	13.0	0.0175	10.7	1	12.2	09/12/20
B1-13	$00^h40^m37^s.85$	$-01°40'09''.6$	13.7	0.0195	13.7	1	6.1	09/12/20
B1-14	$23^h56^m07^s.82$	$00°32'58''.1$	13.9	0.0222	17.9	1	6.1	09/12/20
B1-15	$21^h26^m57^s.85$	$-08°58'42''.5$	13.5	0.0247	14.9	1	6.1	09/13/20
B1-16	$20^h45^m39^s.75$	$-06°24'36''.1$	13.9	0.027	11.8	1	6.1	09/13/20
B1-17	$21^h17^m06^s.99$	$-07°16'32''.1$	13.7	0.0292	12.6	1	4.27	09/13/20
B1-18	$22^h01^m41^s.64$	$11°51:'24''.4$	13.8	0.0298	16.7	1	3.05	09/13/20
B2-1	$15^h09^m13^s.16$	$52°31'42''.4$	12.4	0.0117	28.3	2	6.1	07/08/20
B2-2	$14^h18^m16^s.87$	$31°39'13''.9$	13.5	0.0142	27.1	2	6.1	07/07/20
B2-3	$14^h36^m39^s.94$	$41°09'37''.3$	13.8	0.0178	30.5	2	6.1	07/08/20
B2-4	$13^h40^m09^s.11$	$36°51'39''.9$	13.7	0.0191	30.5	2	3.66	07/08/20

Table 3.1 ***cont.***

ID	RA	Dec	r (mag)	redshift (z)	Hα EW (Å)	Bin	Aperture (")	Obs date
B2-5	$13^h34^m57^s.27$	$34°02'38''.7$	13.2	0.0236	27.7	2	12.2	07/10/20
B2-6	$14^h01^m41^s.39$	$33°49'36''.6$	13.5	0.0264	20.9	2	12.2	07/10/20
B2-7	$15^h01^m50^s.91$	$47°52'31''.4$	13.7	0.0282	21.2	2	6.1	07/08/20
B2-8	$14^h45^m45^s.11$	$51°34'50''.9$	13.5	0.0296	26.0	2	9.15	07/10/20
B2-09	$01^h46^m25^s.05$	$-09°21'48''.1$	13.7	0.0131	30.9	2	6.1	09/25/20
B2-10	$00^h39^m13^s.41$	$00°51'51''.0$	12.4	0.0139	20.4	2	7.32	09/12/20
B2-11	$00^h39^m34^s.83$	$00°51'35''.9$	12.8	0.0146	36.2	2	6.1	09/12/20
B2-12	$01^h33^m01^s.98$	$-01°18'36''.6$	13.8	0.0154	29.2	2	6.1	09/12/20
B2-13	$23^h27^m14^s.80$	$-10°36'46''.8$	13.8	0.016	36.7	2	4.88	09/20/20
B2-14	$00^h39^m35^s.79$	$-10°48'19''.7$	13.2	0.0163	32.5	2	6.1	09/25/20
B2-15	$01^h36^m00^s.16$	$00°39'48''.7$	13.2	0.0172	36.7	2	6.1	09/25/20
B2-16	$00^h23^m59^s.39$	$15°46'13''.6$	13.8	0.0177	20.0	2	6.1	09/12/20
B2-17	$01^h59^m11^s.34$	$00°06'35''.2$	13.9	0.0193	33.0	2	6.1	09/25/20
B2-18	$23^h51^m06^s.26$	$01°03'24''.2$	13.3	0.027	31.4	2	3.05	09/13/20
B3-1	$14^h00^m45^s.76$	$59°19'42''.5$	12.1	0.0101	47.8	3	27.45	06/23/20
B3-2	$14^h28^m24^s.87$	$32°23'40''.6$	13.4	0.0138	54.1	3	6.1	07/07/20
B3-3	$14^h02^m36^s.08$	$32°30'37''.6$	13.0	0.0145	55.8	3	12.2	07/08/20
B3-4	$15^h52^m52^s.84$	$40°38'48''.2$	13.4	0.0153	49.1	3	9.15	07/10/20
B3-5	$13^h26^m09^s.14$	$35°56'03''.9$	12.7	0.0187	42.1	3	9.15	07/07/20
B3-6	$13^h20^m35^s.41$	$34°08'21''.8$	13.9	0.0231	54.6	3	15.25	06/23/20
B3-7	$14^h19^m35^s.30$	$36°08'26''.4$	13.8	0.0247	86.2	3	6.1	07/10/20
B3-08	$23^h30^m13^s.65$	$15°45'39''.7$	13.6	0.0139	43.1	3	6.1	09/13/20
B3-09	$23^h17^m36^s.40$	$14°00'04''.4$	13.9	0.0147	94.0	3	6.1	09/20/20
B3-10	$01^h01^m19^s.48$	$-10°09'17''.0$	13.7	0.0153	51.8	3	4.88	09/25/20
B3-11	$23^h28^m52^s.69$	$-09°21'12''.6$	13.7	0.0162	48.5	3	4.88	09/20/20
B3-12	$21^h12^m24^s.68$	$11°24'31''.2$	13.4	0.0166	41.0	3	4.27	09/20/20
B3-13	$1^h26^m32^s.33$	$12°11'03''.8$	13.7	0.0175	40.4	3	4.27	09/20/20
B3-14	$00^h53^m29^s.92$	$-09°13'55''.9$	13.7	0.019	48.4	3	6.1	09/25/20

Table 3.1 ***cont.***

ID	RA	Dec	r (mag)	redshift (z)	Hα EW (Å)	Bin	Aperture (")	Obs date
B3-15	$23^h44^m02^s.06$	$00°30'59''.8$	12.9	0.0225	45.0	3	6.1	09/20/20
B3-16	$01^h23^m13^s.71$	$-01°36'53''.0$	13.7	0.0249	48.2	3	3.05	09/13/20
B3-17	$20^h45^m14^s.60$	$-06°30'56''.5$	13.7	0.0269	41.8	3	3.05	09/25/20

These targets were observed at WMO for a total of ten or fifteen minutes in each of the three filters. The frames were processed with regular IRAF tasks and were each overscan, zero, dark, and flat corrected.

I did the photometry for these objects in the program Mira. Photometry for each object was done twice with two different apertures, one to circle all the light of the galaxy and one to identify only the nucleus of the galaxy. The aperture I ended up using was the smaller one that encompassed only the nucleus of the galaxy.

With the photometry done, I was able to calculate the ratio from the red-sloping (RS) and blue-sloping (BS) filters. The resulting counts from each aperture I will write as

$$BS_{total} = \text{the sum from each BS image}$$
$$RS_{total} = \text{the sum from each RS image}$$
$$C_{total} = \text{the sum from each C image} \quad .$$

I first calculated the flux per nanometer from the continuum filter with the below equation:

$$C_\lambda = \frac{C_{total}}{\text{FWHM}_C}$$

where C_λ is the flux from the continuum filter per nm and FWHM_C is the full width at half max of the continuum filter, in nm.

The amount of flux present in the BS and RS filters that came from the continuum of the object, C_{BS} and C_{RS}, respectively, can be calculated with

$$C_{BS} = C_\lambda \sum T_{BS} \quad ,$$
$$C_{RS} = C_\lambda \sum T_{RS} \quad ,$$

where T_{BS} and T_{RS} are the transmission (as a fraction) through the BS and RS filters, respectively. The amount of flux in the BS and RS filters from the emission line, BS_{net} and RS_{net}, is then

$$BS_{net} = BS_{total} - C_{BS} \quad ,$$
$$RS_{net} = RS_{total} - C_{RS} \quad .$$

BS_{net} and RS_{net} are then used to calculate the BS/RS ratio, like so:

$$BS/RS = \frac{BS_{net}}{RS_{net}} \quad .$$

3.2 Results and Discussion

A graph of the BS/RS ratios against the SDSS values of redshift (cz) for each object is shown in Figure 3.2 in the orange data points. I created a best-fit line based on those values. The line is shown graphically in Figure 3.2 and follows the equation

$$cz = 56,492.35(BS/RS)^3 - 142,067.09(BS/RS)^2 + 105,464.80(BS/RS) - 15,972.32 \quad . \quad (3.1)$$

To account for the color of each object, a correction factor needed to be added to the BS/RS value with the form

$$BS/RS_{corr} = BS/RS + C * 10^{r'-i'} \quad , \quad (3.2)$$

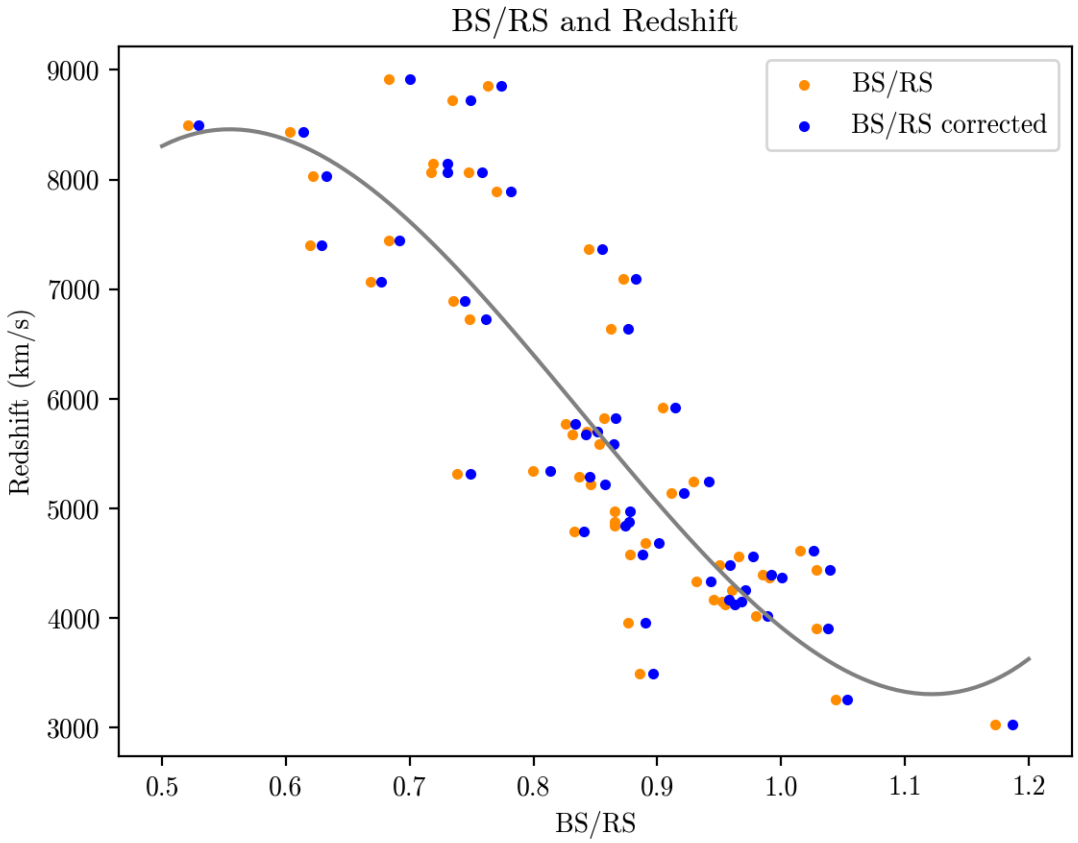

Figure 3.2 This shows the BS/RS ratio plotted in orange against the redshift from SDSS for each object. A best fit line, Equation 3.1, is shown. As described in the text, a correction factor was calculated for the BS/RS values, taking into account the i' and r' magnitudes for each object. This correction factor was then used to minimize the resultant error from the best fit line. The blue data points are the BS/RS values after having the correction factor taken into account.

where r' and i' are the magnitudes of each object in the SDSS r' and i' filters and C is a constant that I solved for empirically.

The constant, C, was determined by finding the value that would minimize the error from the best fit line. This gave the value

$$C = 0.004 \quad .$$

So, the corrected value of BS/RS is

$$BS/RS_{corr} = (BS/RS) + 0.004 * 10^{r'-i'} \quad . \tag{3.3}$$

These corrected BS/RS values are plotted on Figure 3.2 in blue. This value then gets plugged into the best fit line, Eq 3.1,

$$cz = 56,492.35(BS/RS_{corr})^3 - 142,067.09(BS/RS_{corr})^2 + 105,464.80(BS/RS_{corr}) - 15,972.32 \quad . \tag{3.4}$$

The error of this equation is $\pm 641.8 \text{km}\cdot\text{s}^{-1}$.

When looking at just Bin 1, objects with emission of an equivalent width between 10Å and 20Å, the equation is

$$cz = 109,590.96(BS/RS_{corr})^3 - 274,876.54(BS/RS_{corr})^2 + 212,209.27(BS/RS_{corr}) - 42,890.90 \tag{3.5}$$

with an error of $633.8 \text{km}\cdot\text{s}^{-1}$.

The Bin 2 equation, for objects with equivalent width between 20Å and 40Å, is

$$cz = 200,914.00(BS/RS_{corr})^3 - 484,358.49(BS/RS_{corr})^2 + 371,379.85(BS/RS_{corr}) - 83,796.16 \tag{3.6}$$

with an error of $635.6 \text{km}\cdot\text{s}^{-1}$.

Objects within Bin 3, with equivalent width higher than 40Å, follow the equation

$$cz = 30,093.20(BS/RS_{corr})^3 - 72,618.36(BS/RS_{corr})^2 + 46,809.99(BS/RS_{corr}) - 446.56 \quad (3.7)$$

which has an error of 225.0km·s^{-1}.

Figure 3.3 shows the objects split up into Bins 1, 2 and 3 with the lines for equations 3.5, 3.6 and 3.7, respectively.

Based on Figures 3.2 and 3.3, it appears that some of the objects around BS/RS = 0.8 are unnaturally high. This is the [SII] bump that was discussed in subsection 1.6.2. Because the continuum filter was moved from the red side of the ramp filters to the blue side, we no longer had to worry about the [SII] line ending up in the continuum filter. It is, however, still important to consider that the [SII] line would transfer out of the RS filter at z $\approx$ 0.018 and would cause a bump. That variance did introduce some error into the results. More work could be done on objects around that redshift to quantify how the [SII] bump affects the relationship and the error.

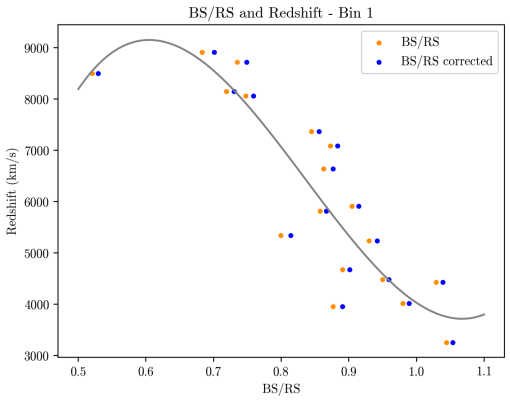

(a) The BS/RS points and the BS/RS corrected values plotted against the SDSS cz for the objects in Bin 1, where the equivalent width is between 10Å and 20Å. The black line is Equation 3.5.

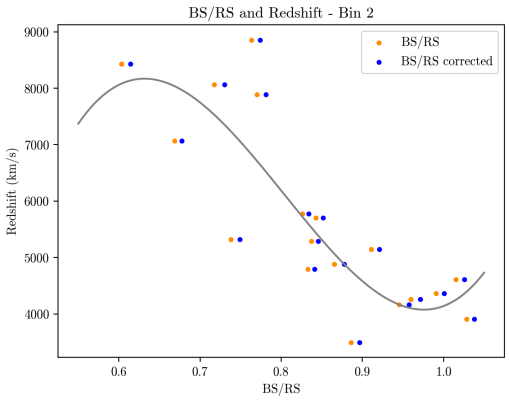

(b) The BS/RS points and the BS/RS corrected values plotted against the SDSS cz for the objects in Bin 2, where the equivalent width is between 20Å and 40Å. The black line is Equation 3.6.

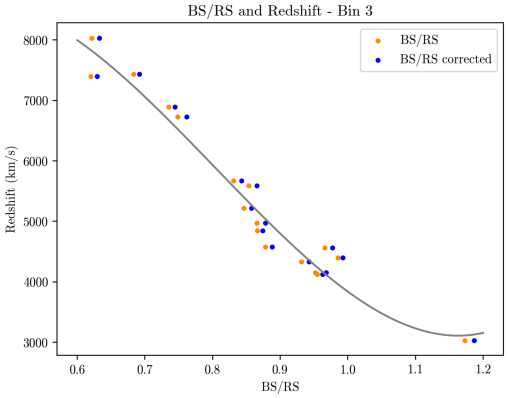

(c) The BS/RS points and the BS/RS corrected values plotted against the SDSS cz for the objects in Bin 3, where the equivalent width is greater than 40Å. The black line is Equation 3.7.

Figure 3.3 Each panel shows the BS/RS points and the corrected values of BS/RS points plotted against the SDSS values of cz for each object, split up by the bins. Equations 3.5, 3.6 and 3.7 are also plotted on each graph.

Chapter 4

Discussion and Conclusions

4.1 Gaussian Filter Confirmation

The objects observed with ARC were a selection from all the groups with Hα emitting galaxies from the GRI plot in Figure 1.5, namely, the Hα, 1σ and 2σ regions. The work of Draper (2019) found that of the 827 SDSS objects in the 2σ range, 78.4% emitted Hα, [OIII] emitters made up 2.4% and the remaining 19.2% had [OII] emission. For the 481 objects in the 1σ region, Draper (2019) found that 91.9% of these had Hα emission, 0.2% were emitting [OIII] and 7.9% had [OII] emission.

With this distribution and a hypothesis following the ΛCDM model, that there is a normal distribution of dwarf galaxies within the voids, a random sampling of objects in the 1σ or 2σ regions would be expected to include a certain percentage of Hα galaxies from within the void. Draper (2019) found that if there were a uniform distribution of galaxies in the voids, then given a random sampling of objects in the 2σ region, 19.2% will have Hα emission (and therefore be within the void), 7.4% will have [OIII] emission and 73.4% will have [OII]. For the same situation,

	Hα	[OIII]	[OII]	Unknown
Prediction	19.2%	7.4%	73.4%	0%
Data	20%	70%	0%	10%

Table 4.1 The predicted and actual values for the types of objects observed within the 2σ region. The predicted values are assuming a uniform distribution of dwarf galaxies in the void.

but instead looking at the 1σ region, Draper (2019) found that 40.0% should have Hα emission, 1.3% should have [OIII] and 58.6% should have [OII].

In this work, for objects within the 2σ region I found that 20% of objects with emission in the bandpass are Hα objects, 70% are [OIII] objects and 0% are [OII] objects, with 10% having emission that could not be identified. These values are compared with the predicted values in Table 4.1.

The similarity between the predicted and actual values for Hα look promising. Unfortunately, the predicted values assumed that any object with Hα emission within the bandpass of the Gaussian filters would be inside a void. Because the transmission of the Gaussian filters does not perfectly align with the location of the voids FN8 and FN2, the objects with Hα emission are actually outside the voids in question. This means that the similarity between the expected and true number of Hα galaxies does not necessarily support the idea that there is a uniform distribution of dwarf galaxies within the void. In contrast, the fact that no objects within the void were found in the sample supports that the voids may be more empty than the concordance model would predict.

A similar comparison for objects in the 1σ region could be made, but unfortunately only one of the five 1σ objects observed had any visible emission, and no statistically significant insights can be gathered from a sample size of one.

These findings suggest that there is not a uniform distribution of dwarf galaxies in the void. In fact, there are likely far fewer than that. This research provided no insight as to whether dark matter

halos that were unable to collect baryonic matter to form galaxies populate the voids observed, so nothing can be inferred as to whether this discrepancy is because of a difference in dark matter or simply baryonic affects.

The main purpose of this work was to investigate the accuracy and usefulness of the Gaussian filter method for determining redshift and identifying emission line galaxies. Keeping this in mind, I calculated how efficiently this method identified emission line galaxies.

In theory, this method should only return galaxies with an emission line within the filter bandpass. In reality, when using the Gaussian filter method, 38.2% of the objects identified actually had emission within the bandpass of the filters. I gathered a random sampling of 500,000 SDSS objects to estimate how likely it is to observe a galaxy with an emission within the bandpass of these filters without using the filters to narrow down the candidates. The redshifts at which the Hα, Hβ, [OIII] or [OII] emission lines would fall into the bandpass (between 6600Å and 6770Å) were calculated. Then the number of objects with one of these emission lines at the respective redshift was identified. With these parameters it was found that, given a random sampling of objects, 7% of them have emission within the bandpass of the filters. This means that, although over 60% of the objects identified as Hα emitters didn't have emission within the bandpass, the method was still effective at identifying objects with emission and greatly decreased the volume of objects needed to sort through to find emission-line galaxies.

The Gaussian filter method can be effectively used to sort through extragalactic objects and determine, with some amount of accuracy, which are emission line galaxies and which are not.

4.2 Ramp Filters

The error of the calculated redshift with this method is 641.8km·s^{-1}. This error is greater than the errors given in Lesser et al. (2019) of 578km·s^{-1} for the simulations with SDSS galaxies and

573km·s^{-1} for the observations of 16 AGN. This could be because this work includes a larger sample size, is focused on regular galaxies rather than AGN or uses a different continuum filter. The continuum filter was altered to improve the method, but more work could be done to determine how it could be affecting the error of this work.

While this work did not show an improvement in the method, it did indicate that the ramp filters method is still effective on larger scales. The error reported above is still an order of magnitude better than other photometric methods, as discussed in Chapter 1.

When analyzing the theory of the ramp filters method, the values of the BS/RS ratios of a group of objects with a spread in redshift should be centered around 1. This is because the filters are mirror symmetric, so as a hypothetical emission line travels through the bandpass with increasing redshift, it starts with BS/RS > 1, then BS flux decreases as RS flux increases until BS/RS = 1, and as BS flux continues to decrease and RS flux similarly increases, eventually BS/RS < 1. The flux through the RS filter at the end should be about the same as the flux of the BS filter at the beginning and vice versa, so the ratio should end at the inverse of its starting value. In this work, that is not what is seen. In Figure 3.2 the observed objects are centered around 0.8 instead of 1.

The simulated and observed objects in Lesser et al. (2019) were centered at 1, but only after use of the correction factor. Without the correction factor, they were centered between 0.7 and 0.8. This means that the BS/RS flux values not being centered on 1 is not a new problem, but one that has, perhaps unwittingly, been corrected for previously with a correction factor. The correction factor in this research was so small, though, that it did not recenter the objects over 1.

But why are these ratio values shifted in the first place? Since the shifting appears in both the observed and simulated objects, the problem likely does not lie with residual sky flux that would be present in my observational data, but taken out of the SDSS data. It is possible that the slope of the continuum is causing the shift in BS/RS values. The correction factor was made to correct for a sloping continuum, in either direction. But, if the continuum of the galaxies are always sloped

in the same direction, it would create an artificially higher flux in the BS or RS filter, making all the ratios shift one way or another. In future work, a focused study of the spectra of these objects could be done to determine if the continuum is sloped in the same direction for all objects and if that could be causing the shift in the BS/RS values.

A valuable benefit of the ramp filters method is that with a wider bandpass of the filters than those used for the Gaussian method, this ramp filter method lets in more light and can be used more easily for survey work. Conducting survey work with these filters is the ultimate goal of this project. Spectroscopy is accurate, but inefficient for survey work. A method with the ability to calculate the distance to a galaxy while conducting a survey of the sky would be a huge benefit to the field of observational cosmology. This analysis has shown that the ramp filters method could be such a method.

To investigate the possible impact of the ramp filter method on sky surveys, consider some calculations that were done to determine how quickly a survey of part of the sky could be completed with the ramp filter method.

The area of sky used for this hypothetical scenario is the Northern Galactic Cap. The Northern Galactic Cap covers about 10,000 square degrees, or one quarter of the sky.

The telescope used would be the ROVOR telescope. This is a 20 inch telescope with a 1 square degree field of view. At first glance, it seems that bigger is better when it comes to telescope diameter, but assuming a given f-ratio, the diameter does not affect the survey time since the diameter is related to the inverse square of the field of view. For example, doubling the diameter increases the light gathered by four times, and therefore decreases the time needed to get to the required magnitude by four. But at the same time, the field of view is decreased by four as well, so four images are needed where one would have been enough with a smaller telescope. Because of that, the time needed to complete the survey evens out despite the telescope size. This means that a small telescope like the 20 inch ROVOR telescope would still work well for survey work.

Primary Mirror	20 inches
Secondary Mirror	4 inches
Mirror reflectivity	80%
Filter transmission	95%
Filter equivalent width	120Å
CCD Window Transmission	80%
CCD QE	90%
Sky brightness	20.8 mag·arcsec^{-2}
Photometric aperture diameter	4 arcsec
Read noise	4 electrons

Table 4.2 Table of parameters used to calculate the exposure time necessary to conduct survey work to a S/N ratio of 8.

All of the following calculations are assuming the values given in Table 4.2.

This survey would observe out to a redshift of cz = 10,000km·s^{-1} or about a distance of 140 Mpc and reach a S/N ratio of 8. With the parameters given in Table 4.2, the exposure time it would take to reach that S/N for a given magnitude is given in Figure 4.1

There are three ways that a survey of the Northern Galactic Cap could be tackled. The first I call the Max-Out method. For this method, we use ROVOR to observe each object in each filter as long as one night will allow, about 6 hours while the object moves from HA = -3 to HA = +3. With this approach, it would take about 18 hours to observe one field in all three filters, which can be approximated to 2 nights of observations per field. With this method, the limiting magnitudes for EW = 10Å, 50Å, 100Å and 250Å would be -16.6 $\pm$ .1, -15 $\pm$ .1, -14.2 $\pm$ .1 and -13.1 $\pm$ .1, as given in Table 4.3. Assuming half the nights of the year are photometric, the time it would take to finish a survey to this depth of the Northern Galactic Cap with the ramp filters is 110 years. This is ridiculously long, so other approaches should be explored.

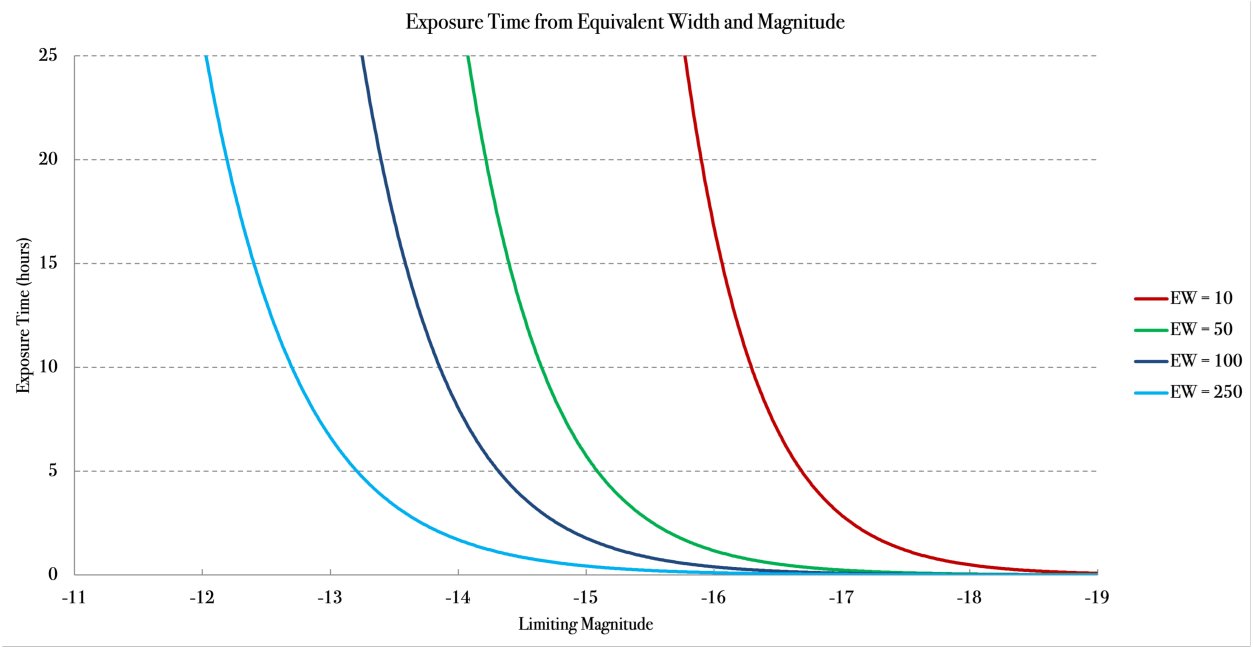

Figure 4.1 The exposure time needed to observe a certain limiting magnitude to a S/N ratio of 8. Each line represents a different equivalent width of the object(s) being observed, as identified in the legend. Created by J. Ward Moody.

Another option I have dubbed the Express Photometry method. For this method, rather than spending six hours on each object with each filter, an object is observed for one hour in each filter. This brightens the limiting magnitude of the survey, but also decreases the time greatly. The limiting magnitudes for EW = 10Å, 50Å, 100Å and 250Å would then be -17.5 $\pm$ .1, -16 $\pm$ .1, -15.4 $\pm$ .1 and -14.3 $\pm$ .1, respectively. These values are given in Table 4.3. A survey of the Northern Galactic Cap using the Express Photometry approach would take 18 years. This is much shorter, but still an unreasonable amount of time.

The final approach, called the Teamwork method, uses the same exposure time as Express Photometry, so the limiting magnitudes are the same. The difference with this method is that five identical telescopes would be used instead of just one. Doing this decreases the expected survey length to 4 years, a much more reasonable amount of time. However, it also greatly increases the cost of such a project. While investing in four additional telescopes seems like a costly endeavour,

	Limiting Magnitude (mag, ± .1)				Total Time
	EW = 10 Å	EW = 50 Å	EW = 100 Å	EW = 250 Å	(years)
Max-out	-16.6	-15	-14.2	-13.1	110
Express Photometry	-17.5	-16	-15.4	-14.3	18
Teamwork	-17.5	-16	-15.4	-14.3	4

Table 4.3 The limiting magnitudes of three methods, given the equivalent width of the object being observed. Column 1 is the method name. Columns 2 through 5 are the limiting magnitudes with equivalent widths of 10Å, 50Å, 100Å and 250Å respectively. The sixth column gives the amount of time it would take this method to survey the Northern Galactic Cap in years.

because the ROVOR telescope has a relatively small diameter the cost is not unreasonable. The entire cost of ROVOR, including the telescope, mount, pier, building and electronics, was less than $200,000, so all the equipment (including ROVOR, which is already purchased) would be less than $1,000,000. This would provide the means to conduct a photometric survey of the Northern Galactic Cap that would identify the redshift of all the emission line galaxies within the survey area and limiting magnitude. Because four years is not near the lifetime of such a telescope array, other projects could be taken on after the completion of this survey, making the monetary cost well worth the scientific benefit.

This hypothetical look at the potential impact of the ramp filter method on current research shows that, while such a survey may not look exactly as described, it is possible to implement this method in a reasonable way that could produce useful results.

Appendix A

ARC Finder Charts

This appendix contains finder charts for all the objects observed with the ARC 3.5-meter telescope and DIS at APO for the Gaussian filter project. The finder charts were made using an online tool created by Eric Jensen, using images from the Digitized Sky Survey. There are 32 finder charts displayed in Figures A.1, A.2, A.3, A.4 and A.5.

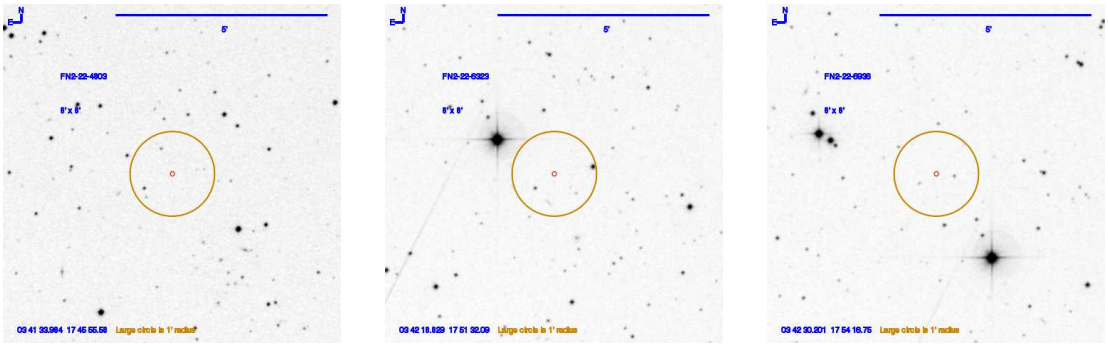

(a) Finder chart for FN2-22-4803.

(b) Finder chart for FN2-22-6323.

(c) Finder chart for FN2-22-6323.

Figure A.1 Finder Charts for some of the objects observed with the ARC 3.5-meter.

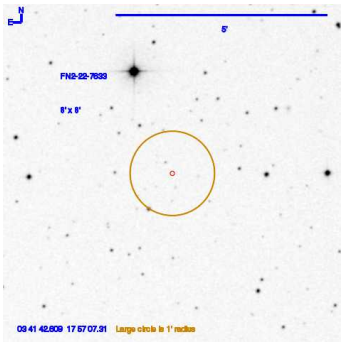

(a) Finder chart for FN2-22-7633.

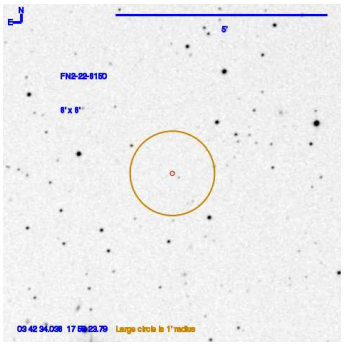

(b) Finder chart for FN2-22-8150.

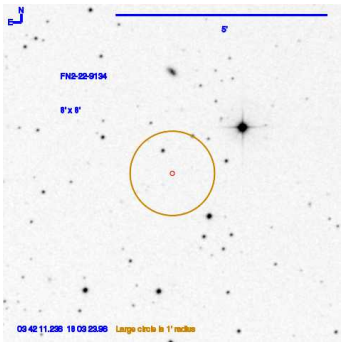

(c) Finder chart for FN2-22-9134.

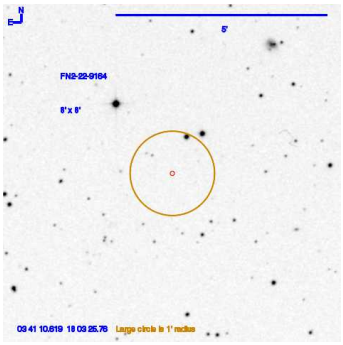

(d) Finder chart for FN2-22-9164.

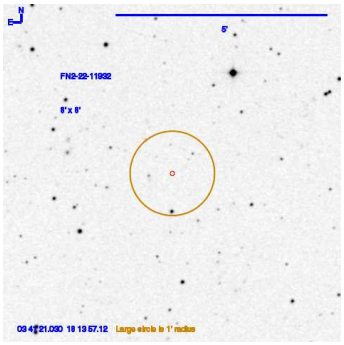

(e) Finder chart for FN2-22-11932.

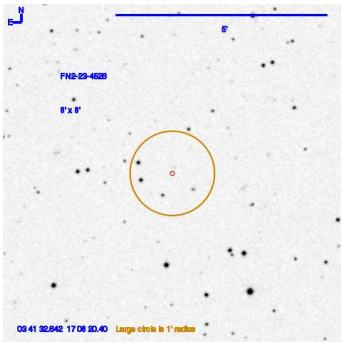

(f) Finder chart for FN2-23-4526.

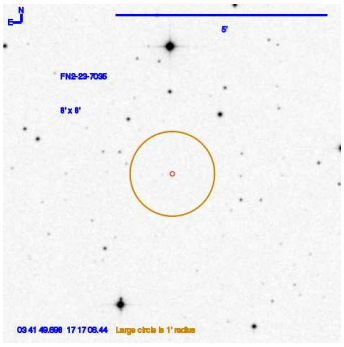

(g) Finder chart for FN2-23-7035.

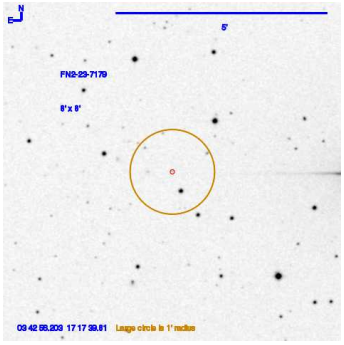

(h) Finder chart for FN2-23-7179.

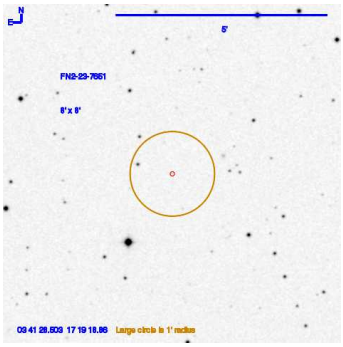

(i) Finder chart for FN2-23-7651.

Figure A.2 Finder Charts for some of the objects observed with the ARC 3.5-meter.

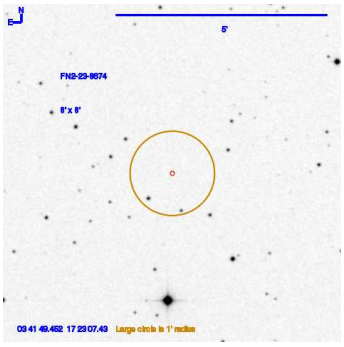

(a) Finder chart for FN2-23-8674.

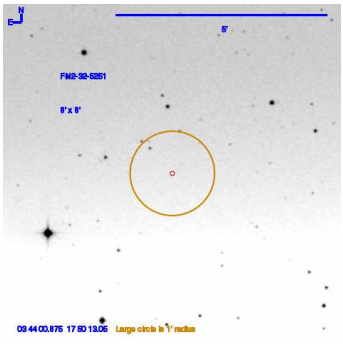

(b) Finder chart for FN2-32-5251.

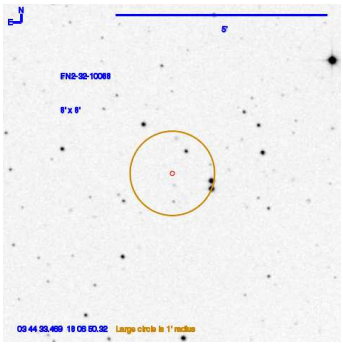

(c) Finder chart for FN2-32-10088.

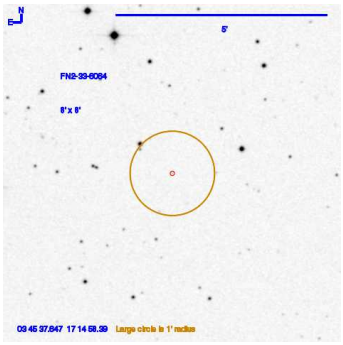

(d) Finder chart for FN2-33-6064.

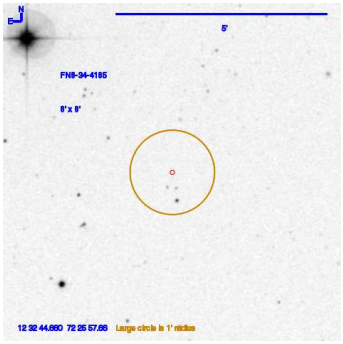

(e) Finder chart for FN8-34-4185.

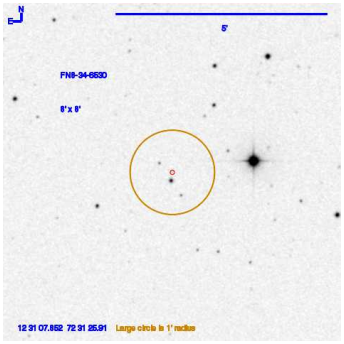

(f) Finder chart for FN8-34-6530.

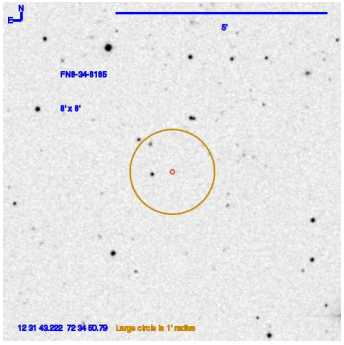

(g) Finder chart for FN8-34-8185.

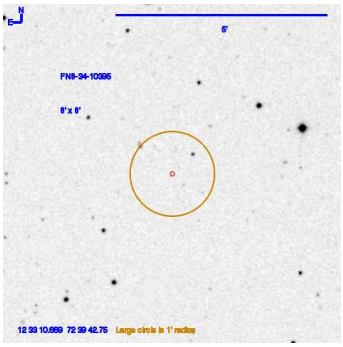

(h) Finder chart for FN8-34-10395.

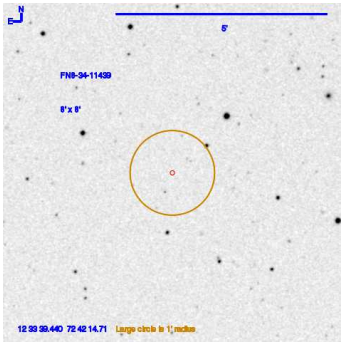

(i) Finder chart for FN8-34-11439.

Figure A.3 Finder Charts for some of the objects observed with the ARC 3.5-meter.

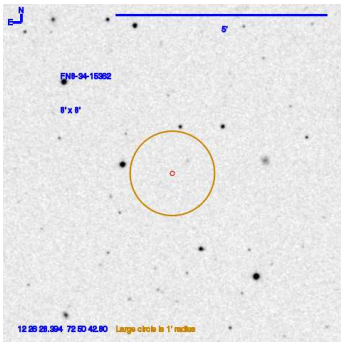

(a) Finder chart for FN8-34-15362.

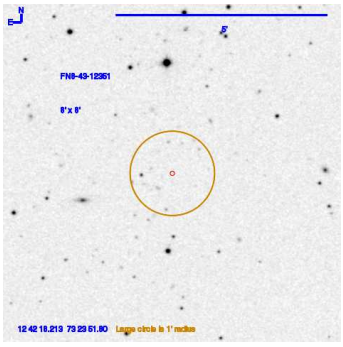

(b) Finder chart for FN8-43-12351.

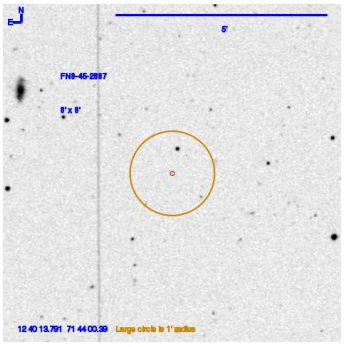

(c) Finder chart for FN8-45-2887.

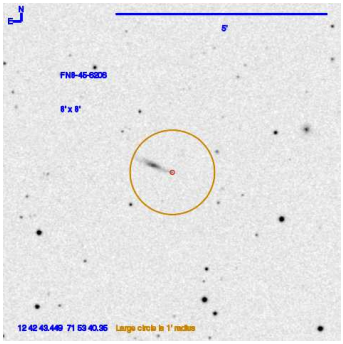

(d) Finder chart for FN8-45-6206-k.

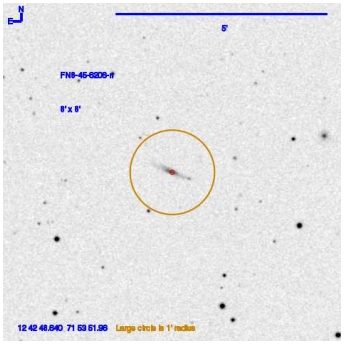

(e) Finder chart for FN8-45-6206-n.

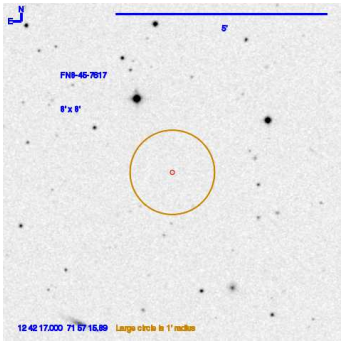

(f) Finder chart for FN8-45-7617.

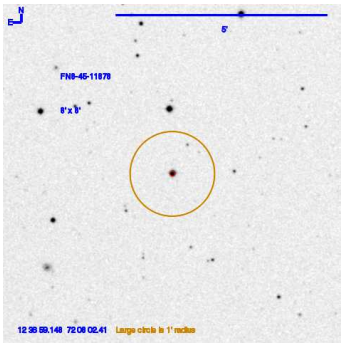

(g) Finder chart for FN8-45-11878.

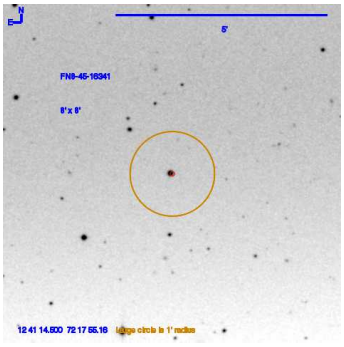

(h) Finder chart for FN8-45-16341.

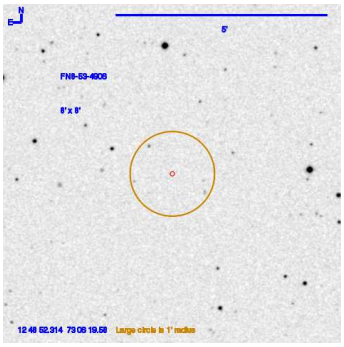

(i) Finder chart for FN8-53-4906.

Figure A.4 Finder Charts for some of the objects observed with the ARC 3.5-meter.

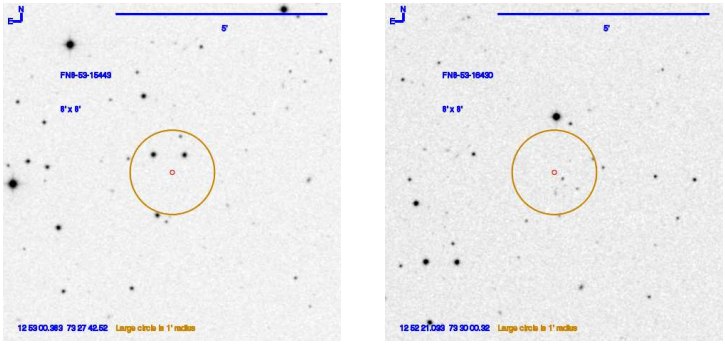

(a) Finder chart for FN8-53-15443.

(b) Finder chart for FN8-53-16430.

Figure A.5 Finder Charts for some of the objects observed with the ARC 3.5-meter.

Appendix B

Ramp Filter Finder Charts

This appendix contains finder charts for all the objects observed with the ramp filters at WMO. The finder charts were made using an online tool created by Eric Jensen, using images from the Digitized Sky Survey. There are 53 finder charts displayed in Figures B.1, B.2, B.3, B.4, B.5, B.6 and B.7.

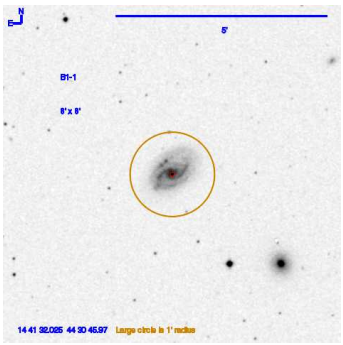

(a) Finder chart for B1-1.

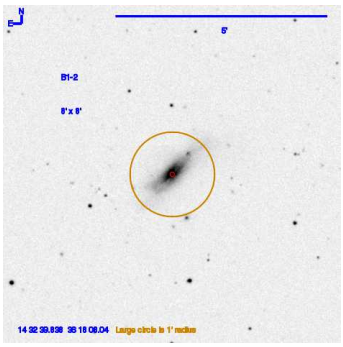

(b) Finder chart for B1-2.

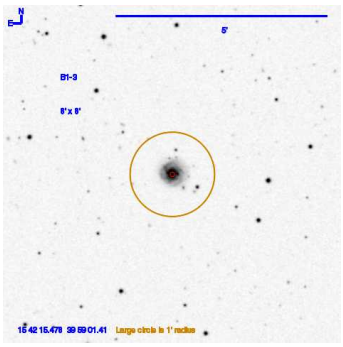

(c) Finder chart for B1-3.

Figure B.1 Finder charts for some of the objects observed with the ramp filters at WMO.

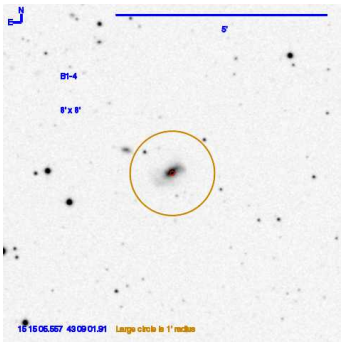

(a) Finder chart for B1-4.

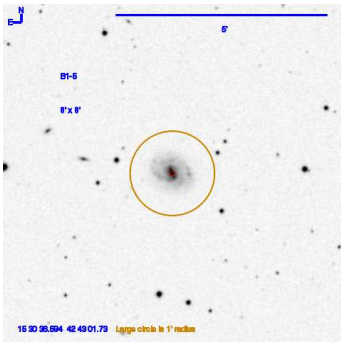

(b) Finder chart for B1-5.

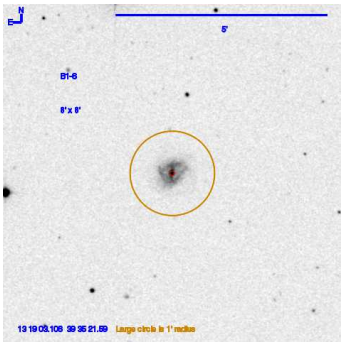

(c) Finder chart for B1-6.

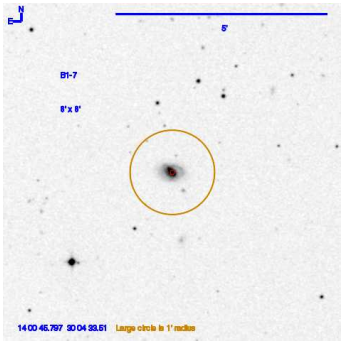

(d) Finder chart for B1-7.

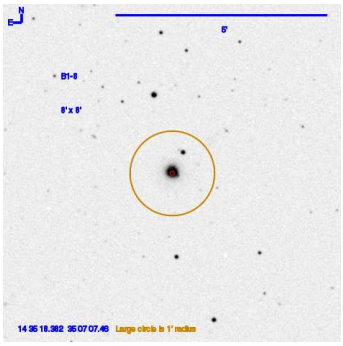

(e) Finder chart for B1-8.

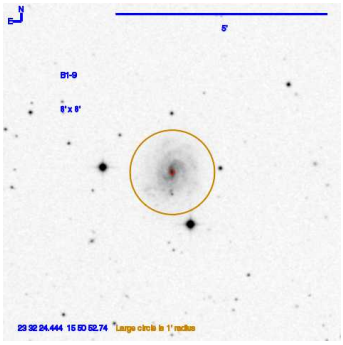

(f) Finder chart for B1-9.

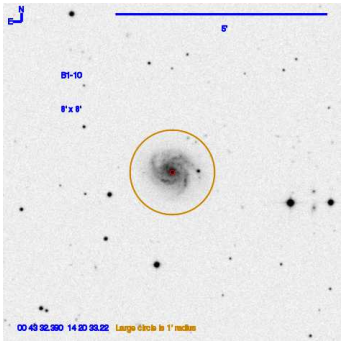

(g) Finder chart for B1-10.

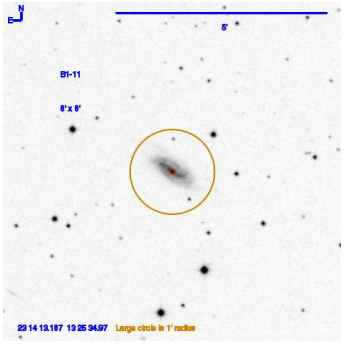

(h) Finder chart for B1-11.

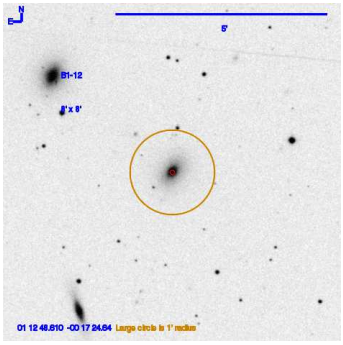

(i) Finder chart for B1-12.

Figure B.2 Finder charts for some of the objects observed with the ramp filters at WMO.

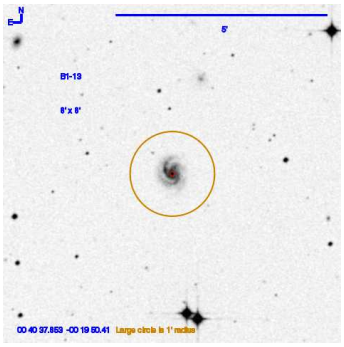

(a) Finder chart for B1-13.

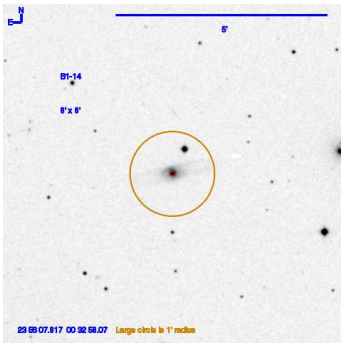

(b) Finder chart for B1-14.

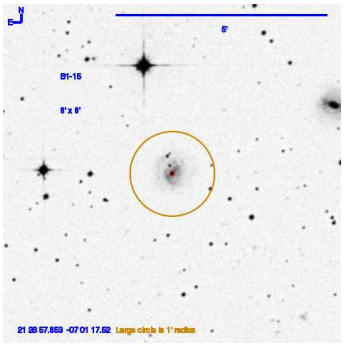

(c) Finder chart for B1-15.

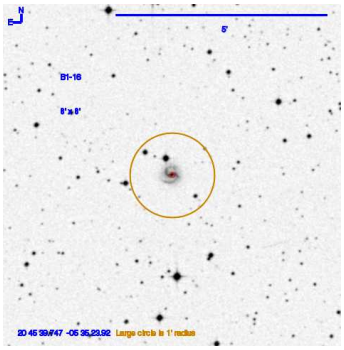

(d) Finder chart for B1-16.

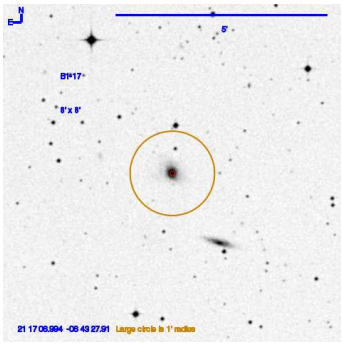

(e) Finder chart for B1-17.

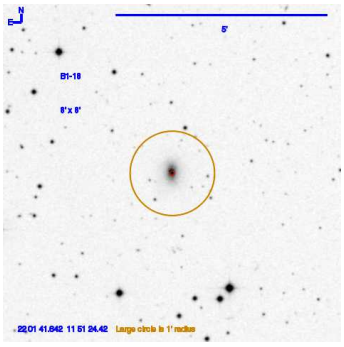

(f) Finder chart for B1-18.

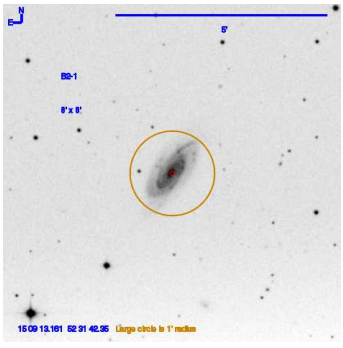

(g) Finder chart for B2-1.

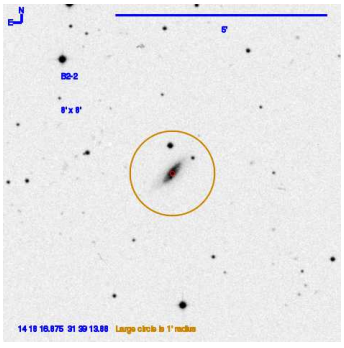

(h) Finder chart for B2-2.

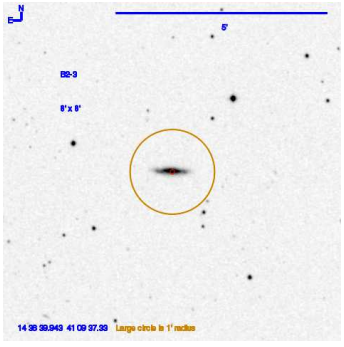

(i) Finder chart for B2-3.

Figure B.3 Finder charts for some of the objects observed with the ramp filters at WMO.

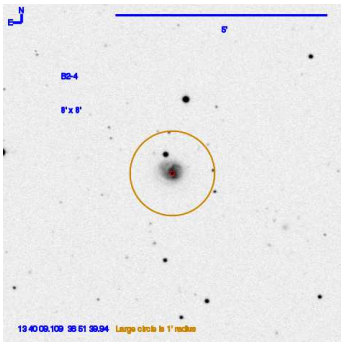

(a) Finder chart for B2-4.

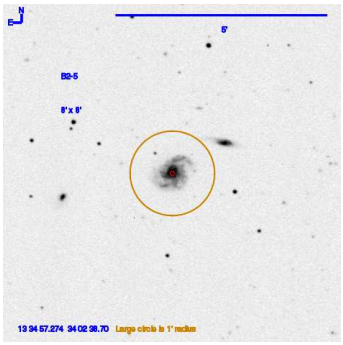

(b) Finder chart for B2-5.

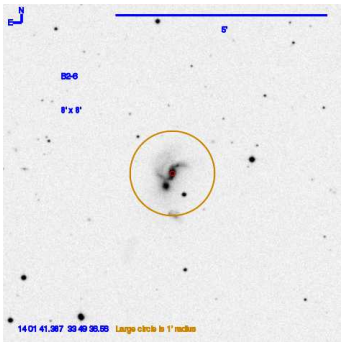

(c) Finder chart for B2-6.

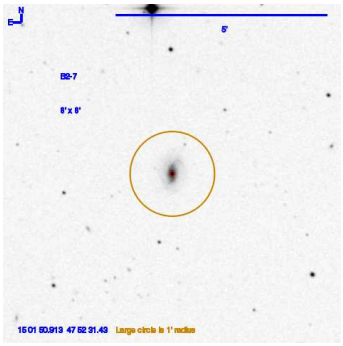

(d) Finder chart for B2-7.

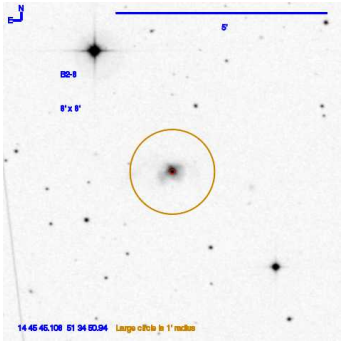

(e) Finder chart for B2-8.

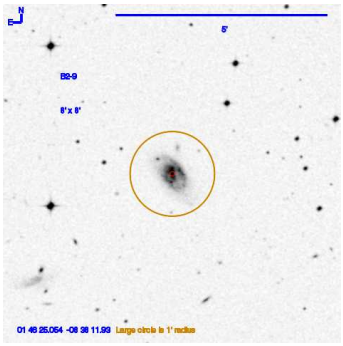

(f) Finder chart for B2-9.

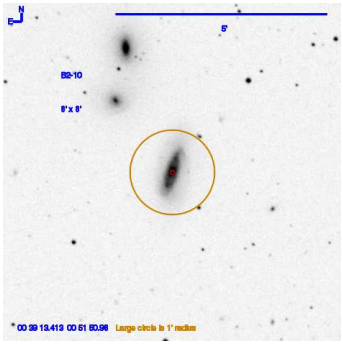

(g) Finder chart for B2-10.

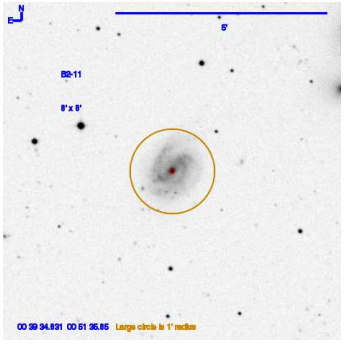

(h) Finder chart for B2-11.

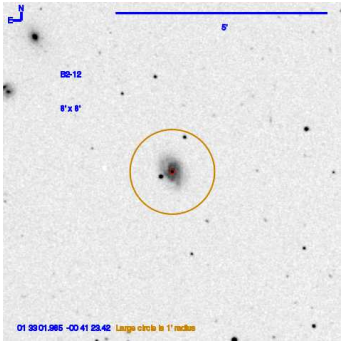

(i) Finder chart for B2-12.

Figure B.4 Finder charts for some of the objects observed with the ramp filters at WMO.

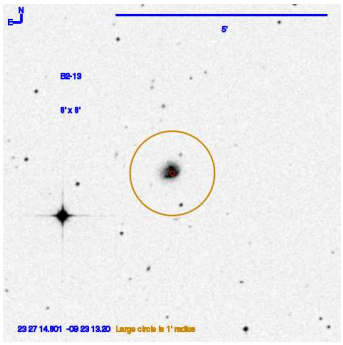

(a) Finder chart for B2-13.

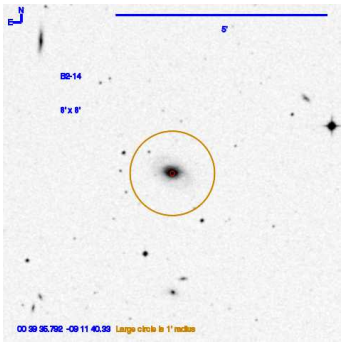

(b) Finder chart for B2-14.

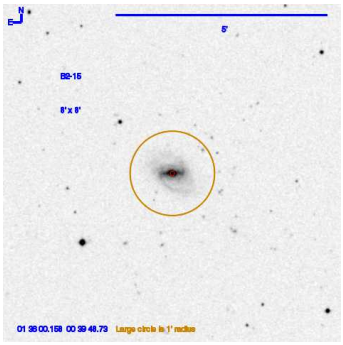

(c) Finder chart for B2-15.

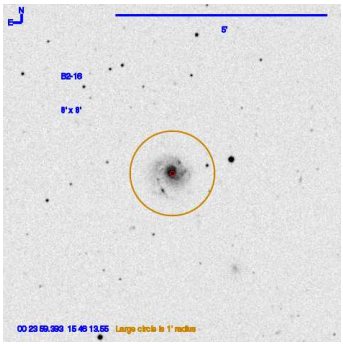

(d) Finder chart for B2-16.

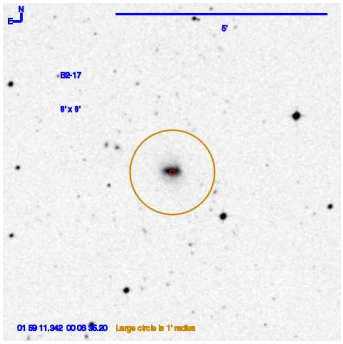

(e) Finder chart for B2-17.

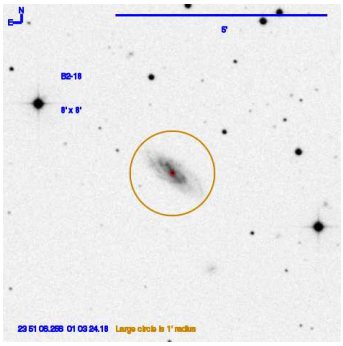

(f) Finder chart for B2-18.

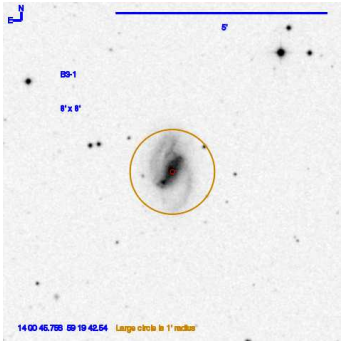

(g) Finder chart for B3-1.

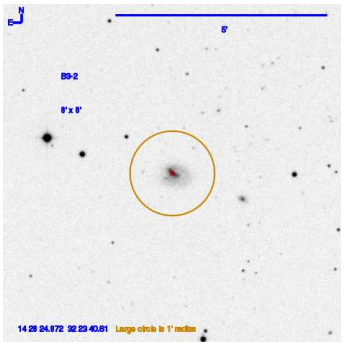

(h) Finder chart for B3-2.

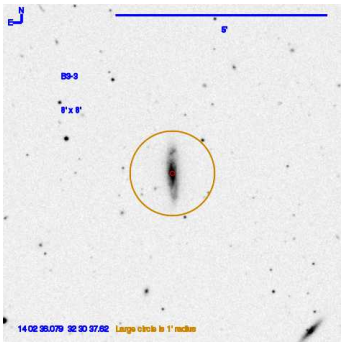

(i) Finder chart for B3-3.

Figure B.5 Finder charts for some of the objects observed with the ramp filters at WMO.

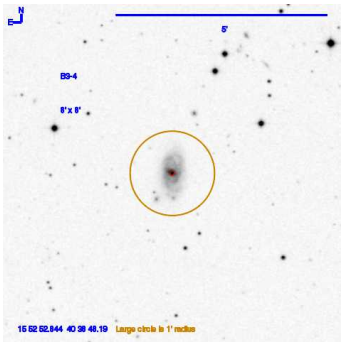

(a) Finder chart for B3-4.

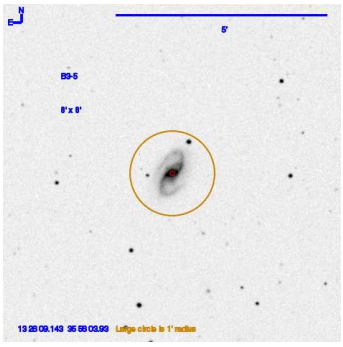

(b) Finder chart for B3-5.

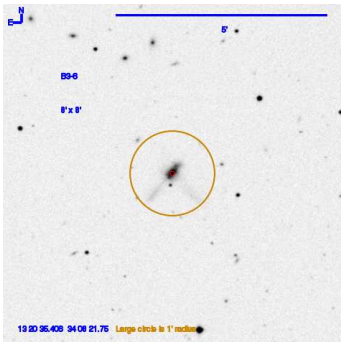

(c) Finder chart for 3-6.

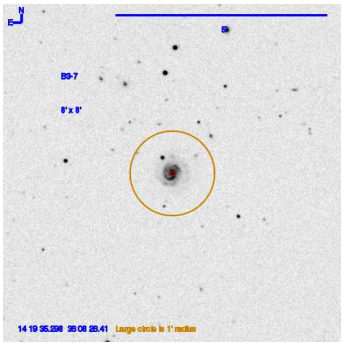

(d) Finder chart for B3-7.

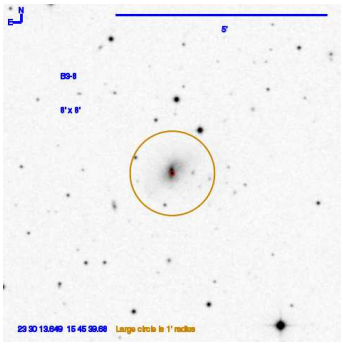

(e) Finder chart for B3-8.

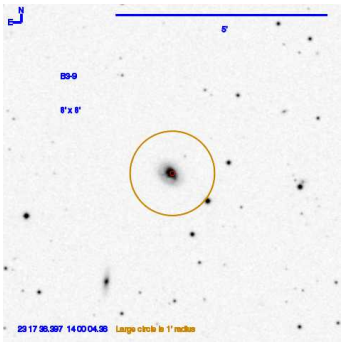

(f) Finder chart for B3-9.

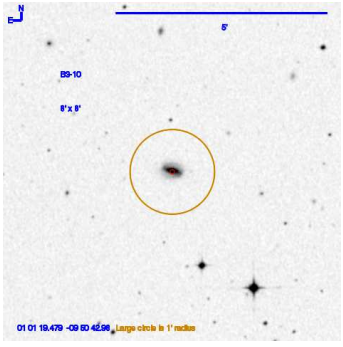

(g) Finder chart for B3-10.

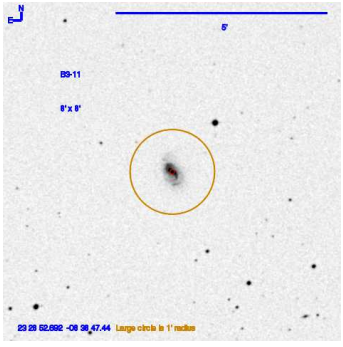

(h) Finder chart for B3-11.

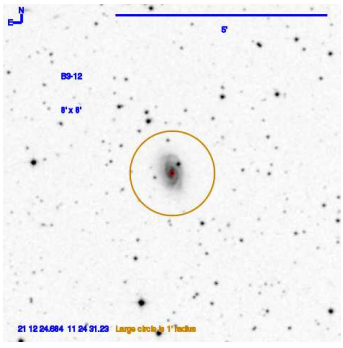

(i) Finder chart for B3-12.

Figure B.6 Finder charts for some of the objects observed with the ramp filters at WMO.

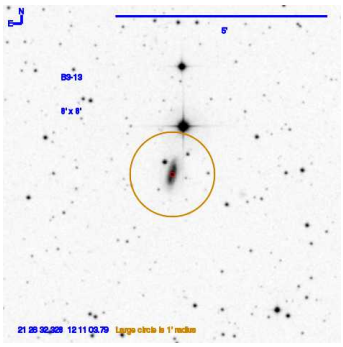

(a) Finder chart for B3-13.

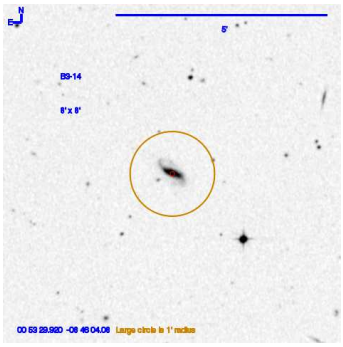

(b) Finder chart for B3-14.

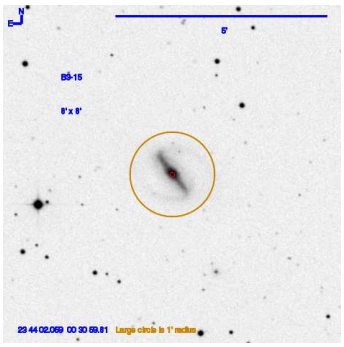

(c) Finder chart for 3-15.

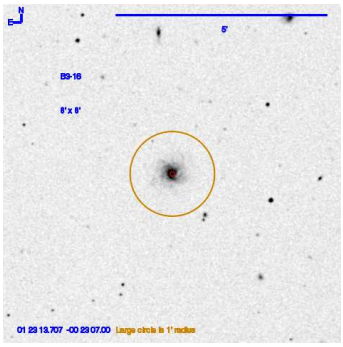

(d) Finder chart for B3-16.

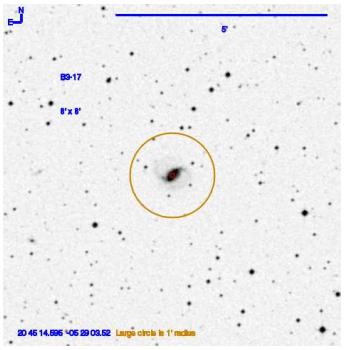

(e) Finder chart for B3-17.

Figure B.7 Finder charts for some of the objects observed with the ramp filters at WMO.

Bibliography

Abolfathi, B., et al. 2018, ApJS, 235, 42

Baum, W. 1962, in Problems of Extra-Galactic Research, Vol. 15, 390

Blanton, M. R., et al. 2017, AJ, 154, 28

Blumenthal, G. R., et al. 1984, Nature, 311, 517

Bode, P., Ostriker, J. P., & Turok, N. 2001, ApJ, 556, 93

Bolzonella, M., Miralles, J.-M., & Pelló, R. 2000, AA, 363, 476

Boylan-Kolchin, M., Bullock, J. S., & Kaplinghat, M. 2011, Mon. Not. R. Astron. Soc., 415, L40

Collister, A. A., & Lahav, O. 2004, PASP, 116, 354

Connolly, A., et al. 1995, AJ, 110

Draper, C. D. 2019, PhD thesis, Brigham Young University

Draper, C. D., et al. in prep, (in prep)

Foster, C., & Nelson, L. A. 2009, Astrophys. J., 699, 1252

Hinshaw, G., et al. 2013, ApJS, 208

Hubble, E. 1929, Proceedings of the National Academy of Sciences, 15, 168

Hubble, E., & Humason, M. L. 1931, ApJ, 74, 43

Klypin, A., Kravtsov, A. V., Valenzuela, O., & Prada, F. 1999, ApJ, 522, 82

Lesser, R. W., et al. 2019, AJ, 157, 99

Mateo, M. 1998, Annual Review of Astronomy and Astrophysics, 36, 435

Moore, B., Ghigna, S., Governato, F., Lake, G., Quinn, T., Stadel, J., & Tozzi, P. 1999, ApJ, 524, L19

Nurmi, P., et al. 2013, Monthly Notices of the Royal Astronomical Society, 436, 380–394

Peebles, P. J. 2001, ApJ, 557, 495

Ralchenko, Y., Kramida, A. E., & Reader, J. 2010, NIST Atomic Spectra Database (version 4.0), http://physics.nist.gov/asd, accessed: 2021-10-13, National Institute of Standards and Technology, Gaithersburg, MD

Reed, D. S., et al. 2015, MNRAS, 451, 4413

Simpson, C. M., et al. 2013, MNRAS, 432, 1989

Springel, V., et al. 2005, Nature, 435, 629

Steele, J. 2021, Senior thesis, Brigham Young University

Steele, R. 2019, Senior thesis, Brigham Young University

Tikhonov, A. V., & Klypin, A. 2009, MNRAS, 395, 1915

Tinker, J. L., & Conroy, C. 2009, Astrophys. J., 691, 633

Umemura, M., & Ikeuchi, S. 1985, ApJ, 299, 583

Vittorio, N., & Silk, J. 1984, ApJ, 285, L39